

Synoptic Control over Orographic Precipitation Distributions during the Olympics Mountains Experiment (OLYMPEX)

DAVID J. PURNELL AND DANIEL J. KIRSHBAUM

Department of Atmospheric and Oceanic Sciences, McGill University, Montréal, Québec, Canada

(Manuscript received 20 September 2017, in final form 16 February 2018)

ABSTRACT

The synoptic controls on orographic precipitation during the Olympics Mountains Experiment (OLYMPEX) are investigated using observations and numerical simulations. Observational precipitation retrievals for six warm-frontal (WF), six warm-sector (WS), and six postfrontal (PF) periods indicate that heavy precipitation occurred in both WF and WS periods, but the latter saw larger orographic enhancements. Such enhancements extended well upstream of the terrain in WF periods but were focused over the windward slopes in both PF and WS periods. Quasi-idealized simulations, constrained by OLYMPEX data, reproduce the key synoptic sensitivities of the OLYMPEX precipitation distributions and thus facilitate physical interpretation. These sensitivities are largely explained by three upstream parameters: the large-scale precipitation rate r_{up} , the impinging horizontal moisture flux I , and the low-level static stability. Both WF and WS events exhibit large r_{up} and I , and thus, heavy orographic precipitation, which is greatly enhanced in amplitude and areal extent by the seeder–feeder process. However, the stronger stability of the WF periods, particularly within the frontal inversion (even when it lies above crest level), causes their precipitation enhancement to weaken and shift upstream. In contrast, the small r_{up} and I , larger static stability, and absence of stratiform feeder clouds in the nominally unsaturated and convective PF events yield much lighter time- and area-averaged precipitation. Modest enhancements still occur over the windward slopes due to the local development and invigoration of shallow convective showers.

1. Introduction

The Olympics Mountains of Washington State, located in the U. S. Pacific Northwest, receive some of the heaviest precipitation of any midlatitude location. Their climate is dictated by their position within the wintertime midlatitude storm track, their proximity to a large water body (the Pacific Ocean), and their steep, compact terrain (Fig. 1a). In the cold season, midlatitude cyclones repeatedly make landfall in the region, producing a massive windward enhancement of frontal precipitation. Annual precipitation estimates from the Parameter-Elevation Relationships on Independent Slopes Model (PRISM) of Oregon State University (Daly et al. 2008) shows a maximum of over 6600 mm over windward (west-southwest)-facing peaks and a leeside minimum of around 400 mm (Fig. 1b). Although such estimates are highly uncertain, they suggest remarkable mesoscale gradients in the regional climate.

With their isolated, axisymmetric shape and exposure to persistent moist marine flow, the Olympics provide an excellent natural laboratory for orographic precipitation research. However, sparse precipitation gauges and widespread radar beam blockage have, until very recently, limited observational coverage over this region (e.g., Westrick et al. 1999). As a result, the understanding of Olympics precipitation has been largely based on a combination of available gauges and numerical modeling (e.g., Colle et al. 2000a,b; Minder et al. 2008; Picard and Mass 2017). While PRISM provides high-resolution daily precipitation estimates there, they are poorly constrained by the sparse gauge network and the neglect of radar data in the retrieval algorithm.

In recent years, the Olympics precipitation network has been substantially upgraded. Minder et al. (2008) installed a transect of tipping-bucket gauges across a narrow windward ridge to study submountain-scale precipitation variability. In 2011, an operational radar was also added to the National Weather Service (NWS) Doppler network at Langley Hill, Washington. Located southwest of the Olympics, this radar complements the

Corresponding author: Daniel Kirshbaum, daniel.kirshbaum@mcgill.ca

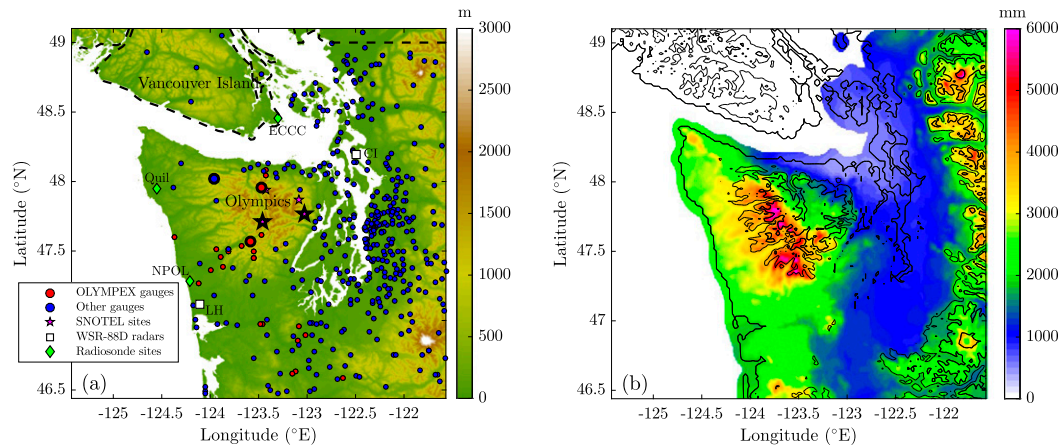


FIG. 1. (a) Terrain map of the Olympics and surrounding regions, along with locations of gauges, radars, and soundings used herein. Dashed line indicates the boundary between the United States and Canada. The Quillayute (QUIL), NPOL, and ECCC sounding sites, along with the Langley Hill (LH) and Camano Island (CI) radars, are indicated. (b) Annual precipitation estimated by PRISM, overlaid on terrain contours of 1, 500, 1000, and 2000 m. The larger, thickly outlined gauges over the Olympics are those selected for the gauge-denial verification experiments of section 3c.

Camano Island radar on the opposite side (Fig. 1a). Building on this newfound infrastructure, the Olympics Mountains Experiment (OLYMPEX) in winter 2015/16 (Houze et al. 2017) intensively observed numerous Olympics precipitation events. OLYMPEX sought to gain process understanding and to verify satellite precipitation retrieval algorithms for the National Aeronautics and Space Administration (NASA) Global Precipitation Measurement (GPM) mission. Its special observational network included, among other instruments, multiple scanning radars, surface precipitation measurements [tipping buckets, Micro Rain Radars (MRRs), etc.], and high-frequency radiosondes. This dense observational network provides a unique opportunity to study Olympics precipitation distributions.

Some general principles of orographic precipitation enhancement (OPE) apply to most mountain ranges, including the Olympics. The amplitude of OPE depends on the impinging vertically integrated horizontal moisture flux (or “influx,” I) (e.g., Neiman et al. 2002). Larger I favors increased terrain-forced condensation and, in turn, precipitation. Also, the nondimensional mountain height ($M = Nh_m/U$, where h_m is the crest height, and N and U are the mean Brunt–Väisälä frequency and mean cross-barrier wind speed in the subcrest layer) broadly controls the dynamical response of the impinging flow (e.g., Smith 1989). Whereas flows with $M < 1$ tend to ascend the barrier with little lateral deflection, flows with $M > 1$ tend to exhibit strong deflection and weakened, upstream-shifted ascent. Also important is the moist instability, which is often quantified by the convective available potential energy

(CAPE). Cumulus convection in moist unstable flows may enhance orographic precipitation, particularly in clouds that would otherwise struggle to produce precipitation via stratiform processes (Cannon et al. 2012).

Another relevant parameter is the upstream precipitation rate r_{up} . When nonorographic “seeder” clouds impinge on a mountain, they stimulate precipitation growth within the orographic “feeder” cloud, thereby enhancing precipitation efficiency compared to clouds that must internally grow particles to precipitation size (e.g., Bergeron 1965). To date, few studies have systematically examined the sensitivity of orographic precipitation to r_{up} . Richard et al. (1987) artificially added snow particles to simulated flows impinging on a 2D ridge representing the Welsh hills. The simulated OPE increased rapidly with r_{up} for small upstream precipitation rates ($< 1 \text{ mm h}^{-1}$) but plateaued at larger values, suggesting that only modest seeding was needed to fully wash out the feeder cloud. In conditionally unstable simulated flows over a narrow tropical island, Kirshbaum and Grant (2012) found that the presence of upstream precipitation (in the form of trade-wind showers) shifted the island precipitation distribution upstream, as impinging clouds and subcloud moisture fluctuations hastened the development of island convection.

While the sensitivities of OPEs are often interpreted based on upstream parameters (e.g., I , M , CAPE, and r_{up}), one may alternatively adopt a synoptic perspective: How does this precipitation depend on the phase of the frontal system in which it is embedded? These two viewpoints are clearly linked because the synoptic state regulates the upstream conditions. However, the

synoptic perspective is arguably more relevant to frontal orographic precipitation, which dominates the Olympics winter climate (Houze et al. 2017). This perspective has been applied in different situations, among them a multiday extreme snowfall event over the Utah Wasatch Mountains (Steenburgh 2003), the microphysics of Northern California precipitation events (Kingsmill et al. 2006), and the sensitivity of cross-barrier precipitation ratios over the Washington Cascades (Mass et al. 2015). Other studies have investigated the synoptic control on cloud microphysics in Cascades precipitation events (Hobbs 1975; Medina et al. 2007).

The objective of this study is to use observations and numerical simulations to quantify and interpret the synoptic controls on orographic precipitation distributions during OLYMPEX. These distributions are evaluated for three different frontal phases: warm frontal (WF), warm sector (WS), and postfrontal (PF). Section 2 presents the observations and section 3 describes a simple spatial precipitation retrieval, the results of which are presented in multievent composites in section 4. Complementary quasi-idealized simulations are described in section 5 and analyzed in section 6. Section 7 provides a summary and conclusions.

2. Observations

a. Standard observations

Hourly gauge accumulations over the Pacific Northwest were obtained from Mesowest (<http://mesowest.utah.edu/>). These include NWS gauges, Remote Automated Weather Stations (RAWS), and snowpack telemetry (SNOTEL) sites, the locations of which are shown in Fig. 1a. Because the majority of the non-SNOTEL gauges lie below the freezing level (which typically varies from 1 to 3 km during Pacific storm landfalls), snow undercatch was not a significant issue.¹ The higher-elevation SNOTEL gauges sample snowier conditions, but their sensors are less prone to undercatch (e.g., Colle and Mass 2000). Rain undercatch is also possible below the freezing level, but its effects were not considered.

Langley Hill and Camano Island Next Generation Weather Radar (NEXRAD) surveillance data were obtained from the U.S. National Climatic Data Center (NCDC). A terrain blockage correction was implemented following Langston and Zhang (2004), which calculates the beam occultation B based on the assumption of a normal distribution of beam energy with 1° half-width at half power. Because of the large degree

of beam blocking in the Olympics, we increased the occultation threshold (beyond which the beam is considered fully blocked) from 0.6 to 0.8. A correction of

$$\Delta \text{dBZ} = 10 \log_{10} \left(\frac{1}{1-B} \right) \quad (1)$$

was then added to the reflectivity (in dBZ) at all times. This correction is shown for the lowest (0.5°) elevation angle of both radars in Figs. 2a and 2b. A composite of the two NEXRADs was then created by defining a Cartesian grid with a 2-km horizontal grid spacing, centered over the Olympics. The reflectivity from the lowest elevation angle with $B < 0.8$ was then interpolated onto this grid. Where data from both radars were available, the data from the radar with the lower beam height were used. The resulting beam height on this grid increases over higher terrain due to beam blockage and increased distance from the radar sites (Fig. 3a).

Operational radiosondes from Quillayute, Washington (QUIL), were also used to sample the upstream flow during frontal periods when the higher-resolution OLYMPEX sondes were not available. Because of their limited temporal resolution, only three such sondes were used.

b. OLYMPEX data

Data from the OLYMPEX field phase (November 2015–January 2016) were used to supplement the gauge observations and to characterize the synoptic-scale evolution of the upstream flow. These include precipitation measurements over and surrounding the Olympics (Fig. 1a) using dual tipping-bucket gauges, Pluvio-2 weighing gauges, MRRs, and disdrometers (Houze et al. 2017). Based on consultation with OLYMPEX scientists (J. Zagrodnik 2016, personal communication), we chose the larger of the two tipping-bucket readings at each site to limit the effects of undercatch. When tipping-bucket data were temporarily unavailable at a given site, we used other available precipitation measurements at that site (Pluvio gauges or disdrometers). Other OLYMPEX data used herein include upstream soundings collocated with the NASA dual-polarization S-band (NPOL) radar along the southwestern Washington coastline, which accounted for 30 of the 33 total soundings (Fig. 1a). While special scanning radars (NPOL, a Doppler on Wheels on the upwind slope, and an Environment and Climate Change Canada radar on Vancouver Island) were also used in OLYMPEX, the coverage of these radars largely overlapped with our NEXRAD radar composite, so for simplicity we did not incorporate them in our retrievals. Also, the gauge network of Minder et al. (2008) was omitted because many of those gauges were buried in

¹ Removing non-SNOTEL gauges above the mean freezing level for each event did not noticeably change the precipitation retrievals in section 3 over the Olympics region (not shown).

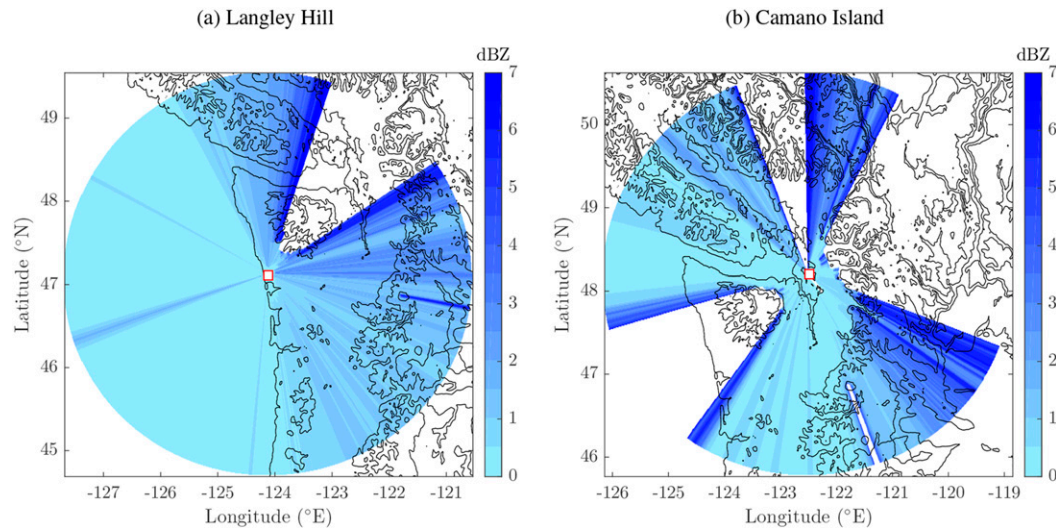


FIG. 2. Partial-blocking corrections applied to (a) Langley Hill (KLGX) and (b) Camano Island (KATX) radar reflectivities. Terrain is contoured at 500, 1000, and 2000 m, and radar locations are shown by the red squares.

snow and not functional for long periods during OLYMPEX.

c. Event classification

Based on the regional NWS surface weather maps, approximately 15 WF, 12 WS, 24 PF, and 14 occluded frontal (OF) periods were observed during OLYMPEX. Although such subjective frontal classifications are very uncertain, they broadly suggest that WF/WS and OF events occurred with similar frequency. We have chosen to focus our analysis on WF, WS, and PF periods and omit OF periods for two reasons: (i) the dynamics of OF passages can be highly complex, and (ii) OF periods share similar prefrontal (postfrontal) signatures to WF (PF) periods.

In our frontal classification scheme, radar reflectivity was first used to bound the time periods of moderate to heavy precipitation (either widespread regions exceeding 20 dBZ or local cells exceeding 30 dBZ). Surface weather maps from the NWS Weather Prediction Center (WPC) were then used to estimate the timings of associated frontal crossings. These classifications were then evaluated using radiosondes, which were inspected for typical upper-air frontal signatures (e.g., [Bluestein and Banacos 2002](#)): (i) a well-defined frontal inversion topped by a deep moist layer, a relatively high tropopause ($z_i > 10$ km), and veering subinversion winds for WF; (ii) deep-layer saturated, nearly moist neutral conditions and nearly unidirectional winds for WS; and

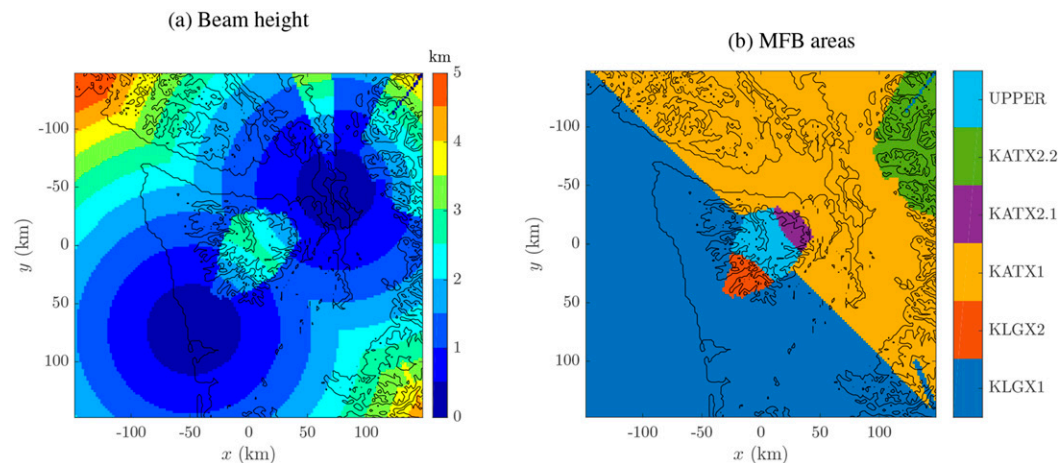


FIG. 3. (a) Height of lowest unblocked radar beam and (b) areas used for MFB correction, both plotted on the Cartesian radar-composite grid. In (b), the names of different areas are defined by the relevant radar (KLGX or KATX) and the elevation angle (1 or 2). The second-lowest elevation angle of KATX is used in two regions, KATX2.1 and KATX2.2. Terrain is contoured at 500, 1000, and 2000 m.

TABLE 1. Timing and sounding information for the 18 OLYMPEX frontal periods.

Event	Year	Start day	Start time	End day	End time	Sounding	Launch day	Launch time(s)
WF1	2015	12 Nov	1700 UTC	13 Nov	0300 UTC	NPOL	12 Nov	1805, 2110 UTC
WS1	2015	13 Nov	0300 UTC	13 Nov	1200 UTC	NPOL	13 Nov	0305, 0610, 0928 UTC
WF2	2015	16 Nov	1900 UTC	17 Nov	1000 UTC	NPOL	17 Nov	0812 UTC
WS2	2015	17 Nov	1000 UTC	17 Nov	1700 UTC	NPOL	17 Nov	1115, 1502 UTC
PF1	2015	18 Nov	0100 UTC	18 Nov	1900 UTC	NPOL	18 Nov	0213, 0515, 1725, 2315 UTC
WF3	2015	3 Dec	0600 UTC	3 Dec	1200 UTC	NPOL	3 Dec	0712 UTC
WS3	2015	3 Dec	1200 UTC	3 Dec	2100 UTC	NPOL	3 Dec	1516, 1915 UTC
PF2	2015	4 Dec	0500 UTC	5 Dec	0000 UTC	NPOL	4 Dec	0514, 1517, 1719 UTC
WF4	2015	5 Dec	1300 UTC	6 Dec	0000 UTC	NPOL	5 Dec	1514, 1913 UTC
WS4	2015	6 Dec	0000 UTC	6 Dec	1300 UTC	NPOL	6 Dec	0517 UTC
WF5	2015	8 Dec	0600 UTC	8 Dec	1300 UTC	NPOL	8 Dec	0713 UTC
WS5	2015	8 Dec	1300 UTC	9 Dec	0000 UTC	NPOL	8 Dec	1515, 1915 UTC
PF3	2015	10 Dec	2300 UTC	11 Dec	1200 UTC	NPOL	11 Dec	0513 UTC
PF4	2015	12 Dec	2200 UTC	14 Dec	0000 UTC	NPOL	13 Dec	0724, 1516, 1916 UTC
PF5	2015	19 Dec	0000 UTC	20 Dec	0000 UTC	NPOL	19 Dec	0215, 0517 UTC
WF6	2016	21 Jan	0400 UTC	21 Jan	1300 UTC	QUIL	21 Jan	1200 UTC
WS6	2016	21 Jan	1300 UTC	22 Jan	0700 UTC	QUIL	22 Jan	0000 UTC
PF6	2016	22 Jan	1600 UTC	24 Jan	0000 UTC	QUIL	23 Jan	0000, 1200 UTC

(iii) surface-based conditional instability, unidirectional or backed low-level winds, and a low tropopause ($z_t < 10$ km) for PF. Radar data were then reevaluated to establish whether the precipitation morphologies were consistent with the frontal phase. Specifically, we sought (i) widespread stratiform precipitation for WF, (ii) ragged patches of nominally stratiform precipitation for WS, and (iii) cellular convection for PF. Narrow cold-frontal rainbands were excluded from the analysis because of their highly transient nature.

Six periods of each frontal phase were analyzed (Table 1), with the classification scheme exemplified for the 3–4 December 2015 period in Fig. 4. As a warm front approached from the west, a sharp frontal inversion descended toward the surface (Figs. 4a,d), accompanied by widespread stratiform precipitation from ~0600 to 1200 UTC (WF3; Fig. 4g). By 1500 UTC, the warm front vanished, and the trailing cold front temporarily stalled (Fig. 4b). Despite the absence of a well-defined warm sector, the deep, surface-based layer of nearly saturated and moist neutral flow and ragged precipitation pattern suggested WS conditions (WS3; Figs. 4e,h). The cold front crossed the Olympics at ~2200 UTC and, after a brief pause in precipitation, conditional instability, low-level wind backing, and cellular convection indicated PF conditions (PF2; Figs. 4c,f,i).

3. Precipitation retrieval

An hourly precipitation retrieval is used to estimate surface precipitation distributions for the different frontal periods. Although this retrieval is more advanced than simple geostatistical methods like kriging with external drift (e.g., Cookson-Hills et al. 2017), it is

substantially simpler than the method of Cao et al. (2018), which used a hydrologic model to estimate high-elevation snowfall during OLYMPEX.

Reflectivity Z from the NEXRAD regional composite, once corrected for partial blocking, is converted to precipitation rate r_{rad} using the Oregon $Z-r$ relation $r_{\text{rad}} = 0.028Z^{0.62}$ from Smith and Krajewski (1993, their Table 1). While attractively simple, the use of a fixed relation for different precipitation types (liquid and frozen, stratiform and convective) is prone to error. Additional errors arise over complex terrain, where substantial OPEs can occur below the radar beam (e.g., Lewis and Harrison 2007). Thus, r_{rad} tends to underestimate the surface precipitation over higher terrain, as illustrated by the comparison of radar-derived and gauge accumulations for WF3 in Figs. 5a and 5b. To reduce these biases, as well as those associated with the radar bright band, radar and gauge data are merged using the two-step process below.

a. Mean-field bias correction

To account for mesoscale radar errors, particularly those near the bright band and over high terrain, we use mean-field bias correction (MFB; e.g., Chumchean et al. 2006). A correction factor in an area A with n gauges is defined as

$$C_{\text{MFB}}(t) = \frac{\sum_{i=1}^n r_{g_i}(t)}{\sum_{i=1}^n r_{\text{rad}_i}(t)}, \quad (2)$$

where r_{g_i} and r_{rad_i} are the gauge and radar hourly precipitation-rate estimates at location i , t is time, and

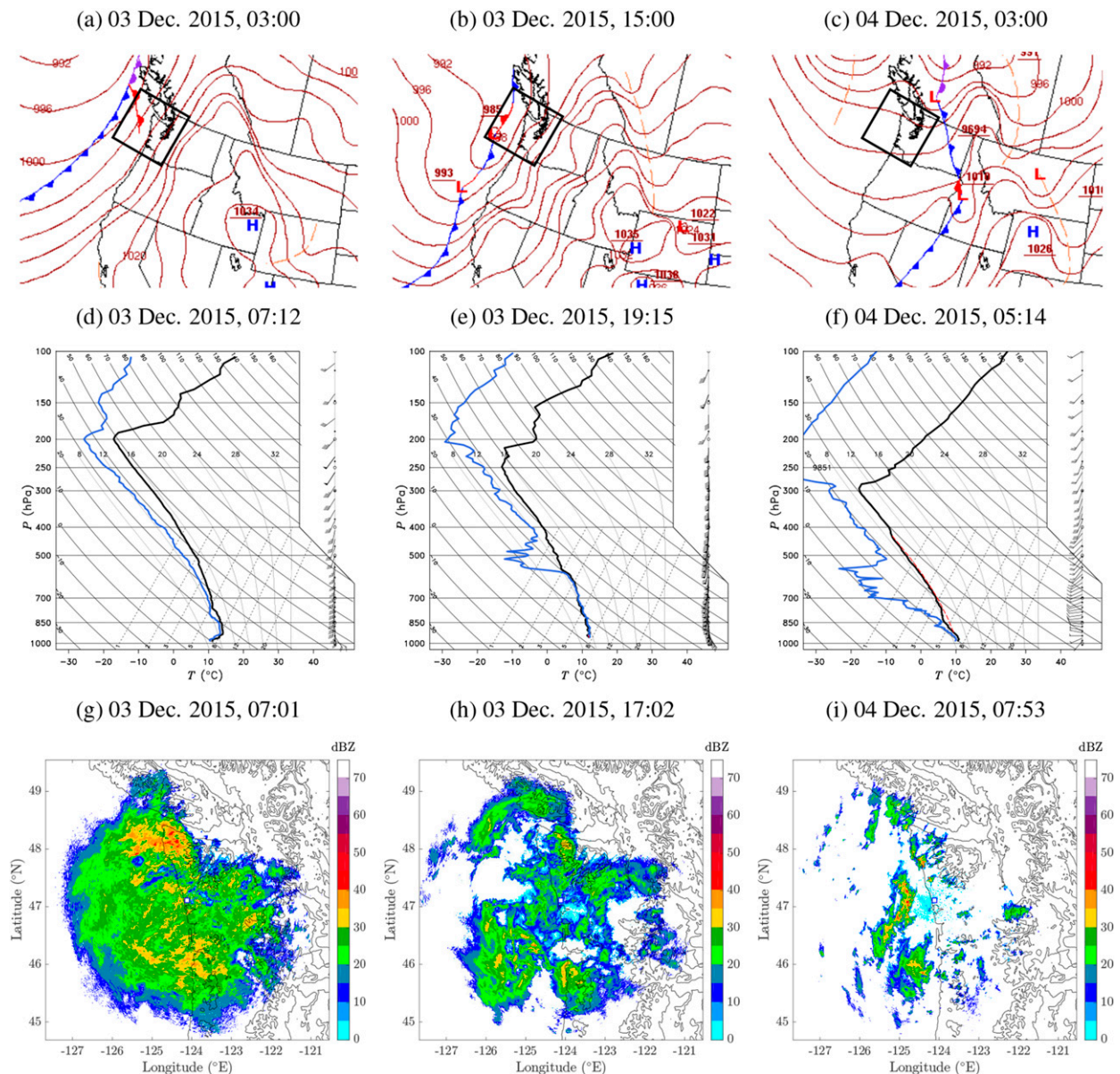


FIG. 4. Example of frontal classification during the passage of a midlatitude cyclone on 3–4 Dec 2015. Sequences of (a)–(c) WPC surface analysis charts, with the region of interest enclosed by a black box, (d)–(f) NPOL soundings, and (g)–(i) NEXRAD radar images from KLGX are shown at selected times during the periods identified in Table 1. (a),(d),(g) correspond to WF3; (b),(e),(h) correspond to WS3; (c),(f),(i) correspond to PF2. All times are in UTC.

$r_{\text{rad},i}$ is averaged over the five grid points closest to the location of $r_{g,i}$. The radar estimate within A is then corrected using $r_{\text{MFB}} = C_{\text{MFB}} r_{\text{rad}}$. The domain is decomposed into different areas based on radar coverage and elevation angle (Fig. 3b). An additional area (UPPER) is defined over the highest Olympics terrain, where the beam height (>3 km) typically exceeds the freezing level. For the WF3 example, the MFB correction is strongly positive over the KLGX2 and UPPER regions (Figs. 5c,d), yielding a more physically plausible precipitation field

over the Olympics with a maximum on its southwestern slopes.

b. 2D-VAR

Additional small-scale corrections are carried out in close proximity to each surface gauge measurement using 2D variational data assimilation (2D-VAR), an optimal-estimation technique that accounts for errors in both radar and gauge measurements. Our implementation closely follows Bianchi et al. (2013, hereafter B13)

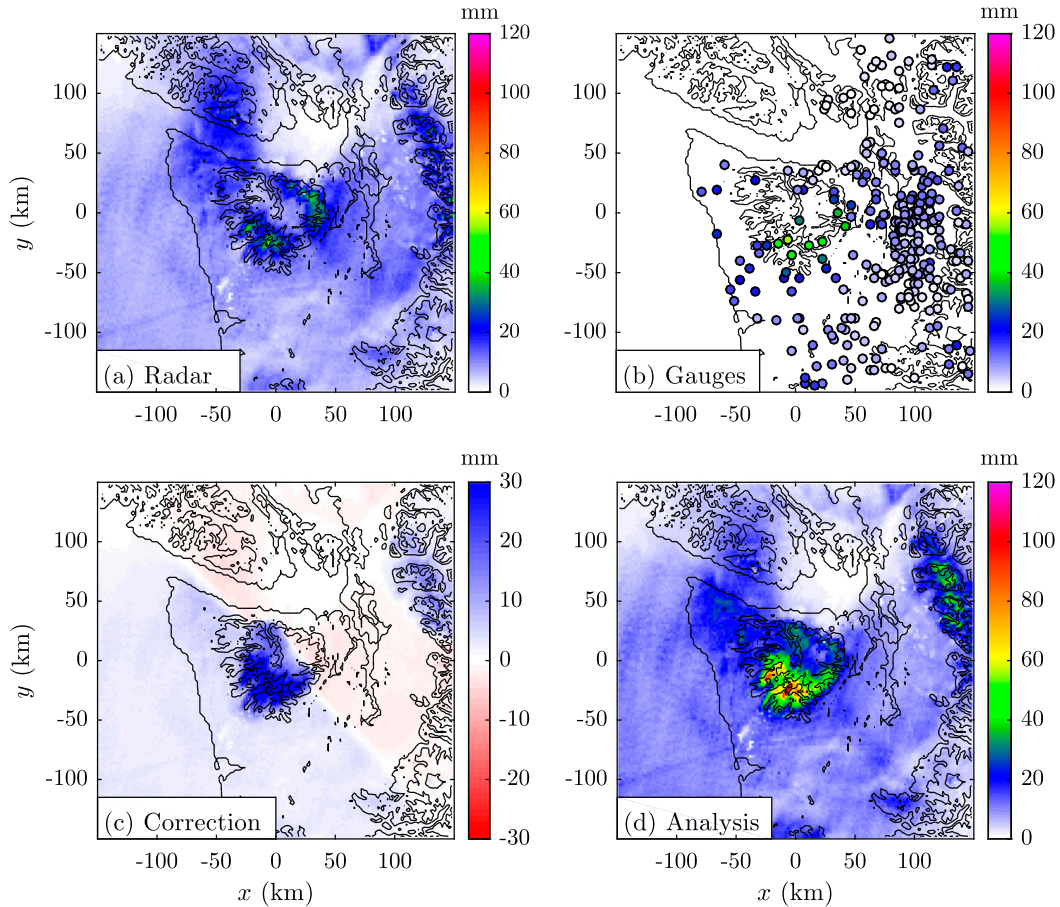


FIG. 5. MFB example for the WF3 period (see Table 1 for timing): (a) radar-derived precipitation accumulation, (b) gauge accumulations, (c) MFB correction, and (d) resulting analysis.

and is presented in detail in the appendix. It is applied only to the WF and WS events, where the precipitation is largely stratiform and the radar reflectivity is highly contaminated by the bright band. In such cases, point gauge measurements may provide useful information about their immediate surroundings, albeit with significant representativity errors. The adjustment is omitted in convective PF events where cumulative precipitation may vary widely over very short distances and bright-band effects are less prominent. For the WF3 example, the 2D-VAR adjustment is generally negative over the Olympics and Cascades Mountains but positive over low-lying areas in between (Figs. 6a,b).

c. Evaluation

Along with the issues already raised at the beginning of section 3, several additional shortcomings render the retrievals uncertain. Many of the gauges are found in valleys (Fig. 1a), where precipitation is typically lighter than that over neighboring ridges (e.g., Minder et al. 2008). Thus, significant underestimates may occur over

the higher terrain. Moreover, because the height of the radar beam above ground level varies widely over complex terrain, the degree of subbeam orographic enhancement does as well, which undermines the assumption of a constant ratio between gauge and radar precipitation in the MFB analyses. Finally, the 5-km decorrelation length scale used in the 2D-VAR analysis (see the appendix), while reasonable over flatter terrain, may spread gauge information too broadly over the Olympics.

We evaluate the retrievals using two different verifications, each with its own limitations. First, we rerun the retrievals with single gauges withheld and then compare the retrieved precipitation at the grid point nearest the withheld gauge to the gauge reading. The five withheld gauges include two SNOTEL gauges, two special OLYMPEX gauges, and one RAWS gauge (Fig. 1a). The root-mean-square error (RMSE) of all hourly samples for each gauge ranges from 2–5 mm h⁻¹ (WF/WS) to 0.5–2 mm h⁻¹ (PF) (Table 2). While these errors are comparable to the corresponding composite precipitation rates (Fig. 7), they should be interpreted with

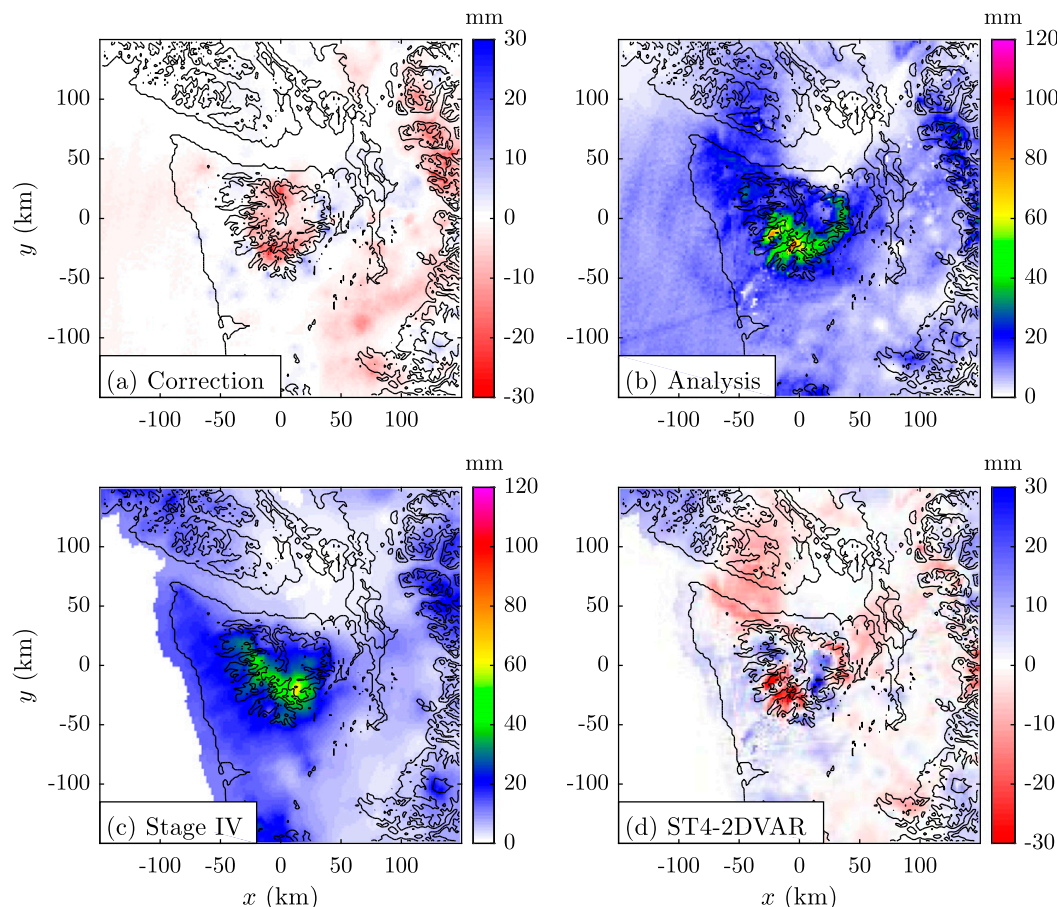


FIG. 6. 2D-VAR example for the WF3 period (see Table 1 for timing): (a) 2D-VAR correction, (b) resulting analysis, (c) Stage-IV analysis of the same period, and (d) difference between Stage-IV analysis and our 2D-VAR analysis. The background state and gauge data used for the retrieval are shown in Figs. 5d and 5b, respectively.

caution. Over the data-sparse Olympics, each gauge produces a large correction to the retrieval. When the gauge is withheld, its large correction becomes incorporated into the error, which inflates the error magnitude.

As a second verification, we compare the retrievals to the National Centers for Environmental Prediction (NCEP) Stage-IV product, a mosaic of regional multi-sensor analyses generated by the NWS River Forecast Centers (RFCs) (Lin and Mitchell 2005). Each RFC uses multiple quality-control measures, including correcting for terrain beam blocking, quality-controlling low-level reflectivities, and bias correction and/or radar calibration. Because these data were only available at 6-h intervals on a coarse polar stereographic grid (with a spacing of 4.7625 km at 60°N) and omitted special OLYMPEX observations, they are not ideal for characterizing OLYMPEX precipitation. However, as a widely used operational product, they are still useful for broadly evaluating our retrievals. This evaluation has

two caveats: (i) the two analyses use some of the same data and are thus not independent, and (ii) all such analyses are uncertain, so neither should be interpreted as ground truth.

Since WF3 coincided with a Stage-IV analysis period, we compare the two analyses for this period directly in Figs. 6b and 6d. They broadly agree except over the Olympics, where our retrieval indicates heavier precipitation over the southwestern Olympics slopes and lighter precipitation over the southeastern and northwestern slopes. For a more quantitative and thorough comparison, we evaluate the normalized root-mean-square difference (NRMSD; Surcel et al. 2014):

$$\text{NRMSD} = \sqrt{\frac{\sum_{i=1}^{N_x} \sum_{j=1}^{N_y} [P_1(x_i, y_j) - P_2(x_i, y_j)]^2}{\sum_{i=1}^{N_x} \sum_{j=1}^{N_y} [P_1(x_i, y_j) + P_2(x_i, y_j)]^2}}, \quad (3)$$

TABLE 2. Verification of retrievals with specific gauges removed over the Olympics against the withheld-gauge readings. For each gauge and event type, the RMSD is calculated over all hourly samples.

Gauge type	Latitude (°N)	Longitude (°E)	Elevation (m)	Event type	RMSE (mm h ⁻¹)
SNOTEL	47.71	-123.46	1476	WF	2.9
				WS	4.5
				PF	2.0
SNOTEL	47.76	-123.03	1231	WF	2.4
				WS	3.1
				PF	0.8
OLYMPEX	47.96	-123.48	1123	WF	2.0
				WS	2.8
				PF	0.8
OLYMPEX	47.57	-123.58	171	WF	1.9
				WS	2.2
				PF	0.9
RAWS	48.02	-123.96	738	WF	2.8
				WS	3.1
				PF	1.4

where P_1 and P_2 are the two cumulative precipitation fields under comparison (with the Stage-IV data interpolated to our 2-km regional grid). An NRMSD of zero (one) means perfect agreement (disagreement) between the two fields. As shown in comparisons of nine frontal periods (three of each type) in Table 3, the NRMSD generally lies between 0 and 0.5 with a mean of 0.33, suggesting reasonable overall agreement but also substantial differences.

4. Observational analysis

The retrieved precipitation distributions for each frontal phase (WF, WS, and PF), averaged over the corresponding six periods listed in Table 1, are presented in Fig. 7. The WS composite has the largest absolute OPE, focused over the high windward slopes of the Olympics. Although the WF composite exhibits the heaviest upstream precipitation, its windward OPE is

weaker and shifted upstream (southwest) relative to the WS composite, and its leeside precipitation suppression is stronger. Precipitation is generally much lighter in the PF composite, with weak OPE along the lower western and southwestern slopes. This maximum extends southward of the Olympics, coinciding with lower hills between the Olympics and the Oregon Coast Range (Fig. 1a).

To relate the observed OPEs to upstream parameters I , M , and r_{up} , we first define \mathbf{u}_m as the water vapor-density (or ρ_v)-weighted mean wind vector over the sounding depth. Then, I is the vertically integrated component of the horizontal moisture flux parallel to \mathbf{u}_m . To calculate M , we vertically average N (computed separately for each level) and the wind component aligned with \mathbf{u}_m from the surface to $h = 2432$ m, the Olympics crest height. The relative humidity (RH) is computed relative to liquid for $T > T_0$ and ice for $T \leq T_0$, where T is temperature and $T_0 = 0^\circ\text{C}$. If RH at a

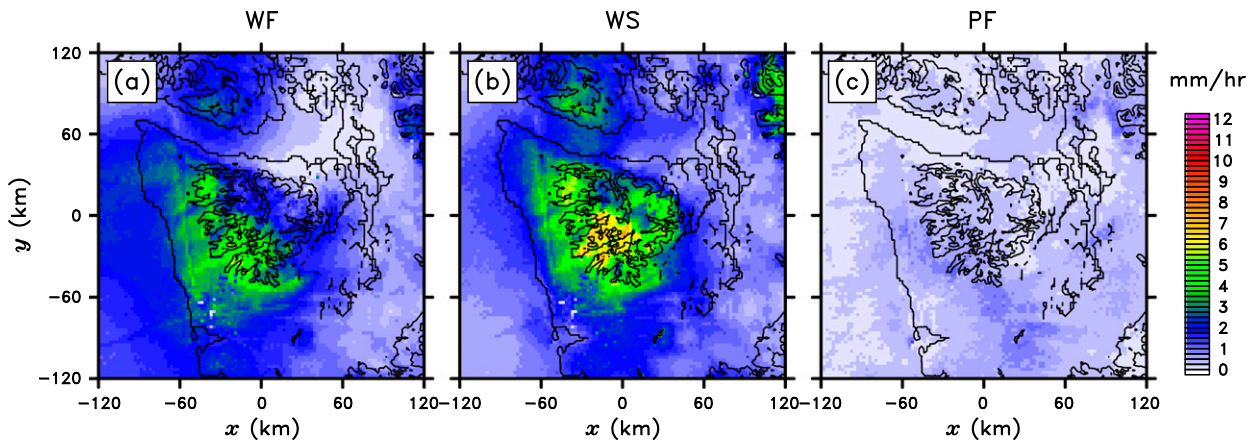


FIG. 7. Composites of mean retrieved precipitation rate during (a) WF, (b) WS, and (c) PF events.

TABLE 3. NRMSD between our precipitation retrievals and Stage-IV analyses for nine selected 6-h periods.

Event	Year	Start day	Start time	End day	End time	NRMSD
WF3	2015	3 Dec	0600 UTC	3 Dec	1200 UTC	0.24
WS3	2015	3 Dec	1200 UTC	3 Dec	1800 UTC	0.25
PF2	2015	4 Dec	0600 UTC	4 Dec	1200 UTC	0.33
WF4	2015	5 Dec	1800 UTC	6 Dec	0000 UTC	0.31
WS4	2015	6 Dec	0600 UTC	6 Dec	1200 UTC	0.32
WF5	2015	8 Dec	0600 UTC	8 Dec	1200 UTC	0.23
WS5	2015	8 Dec	1800 UTC	9 Dec	0000 UTC	0.25
WS5	2015	11 Dec	0000 UTC	11 Dec	0600 UTC	0.49
PF4	2015	13 Dec	0000 UTC	13 Dec	0600 UTC	0.52

given level is greater than 98%, we use the saturated Brunt–Väisälä frequency N_m (Durrán and Klemp 1982) at that level. If not, we use the dry Brunt–Väisälä frequency N_d , evaluated based on the virtual potential temperature θ_v .

To quantify the regional precipitation, we define a cross-barrier transect aligned with \mathbf{u}_m across the geographical center point of the Olympics (47.44°N, –123.49°E), with a length of $2L = 200$ km and a width of 40 km. As a metric for orographic precipitation, we use the drying ratio $DR = P/I$, where

$$P = \int_{-L}^{s_e} \rho_w r_t ds, \quad (4)$$

ρ_w is the density of liquid water, s is distance along the transect ($s = 0$ is the Olympics center point), s_e is the as-yet-unspecified downstream bound of the integral, and $r_t = r_t(s)$ is the precipitation rate averaged over the transect width. To obtain r_{up} , we average r_t along the same transect from the upstream boundary of our grid to $-L$, over which orographic precipitation modification is negligible (as will be shown). The r_{up} thus obtained may be underestimated because at long distances upstream of the radar, the radar beam may overshoot low-level precipitation growth.

While DR is commonly used to quantify orographic precipitation (e.g., Smith and Barstad 2004; Kirshbaum and Smith 2008), it does not necessary isolate OPE because it also includes the contributions of large-scale precipitation. A truer measure of OPE is $DR^* = P^*/I$, where P^* is given by (4) with the integrand r_t replaced by $r_t - r_{up}$. As r_{up} is nonnegative, $DR^* \leq DR$ and can be negative when leeside precipitation suppression exceeds windward precipitation enhancement. In the following, we compute drying ratios for both $s_e = L$ (DR and DR^*) and $s_e = 0$ (DR_w and DR_w^*), the latter focusing on just the windward side of the Olympics.

For a given frontal period, the upstream parameters $|\mathbf{u}_m|$, I , CAPE, and M are calculated for each relevant sounding listed in Table 1, then averaged over all such

soundings, and r_{up} and P are evaluated using the retrieved precipitation field and the diagnosed $|\mathbf{u}_m|$. Given the close proximity of these soundings to the Olympics topography (Fig. 1a), some of them may be orographically modified and thus not entirely representative of the undisturbed flow farther upstream.

As shown in Table 4, the combination of large $|\mathbf{u}_m|$, I , and r_{up} , along with relatively small M and CAPE, in the WF and WS cases favors heavy stratiform precipitation, while the smaller $|\mathbf{u}_m|$, I , and r_{up} , and larger M and CAPE, in the PF cases favor lighter convective precipitation. Because these M calculations are based on the upstream flow, they neglect the impacts of terrain-forced saturation (in the nominally unsaturated PF flow) or desaturation (in the nominally saturated WF/WS flows). The related latent heating effects may substantially impact the “effective” M , and hence, the degree of upstream blocking (e.g., Jiang 2003).

Although the mean DR for each frontal type decreases modestly from WF (0.25) to WS (0.22) to PF (0.18), the associated OPEs are obscured by the widely varying mean r_{up} among these frontal types. This enhancement is clarified by DR^* , which follows a different trend: it is maximized for WS (0.12) and decreases greatly for WF (0.03) and PF (0.01). These generally small DR^* values suggest that the OPEs consume only a small fraction of the impinging moisture flux. The larger DR^* in the WS cases likely stems from their combination of large I and small M , which favors strong terrain-forced uplift of moisture-laden and weakly moist stable impinging flow.

Like DR, DR_w is maximized in WF events and progressively decreases in WS and PF events. While DR_w^* also follows the same basic trend as DR^* , its sensitivity to frontal type is weaker: DR_w^* for WS (0.11) is only slightly larger than that for WF (0.09), suggesting a similar degree of windward enhancement. Thus, the large differences in DR^* between these cases are mainly attributable to stronger leeside precipitation suppression in WF events. This suppression is promoted by

$M \geq 1$ and large r_{up} , which favors large-amplitude mountain wave breaking and strong precipitation evaporation within leeside downdrafts. As with the WF events, $\text{DR}_w^* > \text{DR}^*$ for the PF events due to the exclusion of the leeside rain shadow (Fig. 7c).

The above finding that Olympics precipitation shadows are the strongest in WF events differs with the Cascades study of Siler and Durran (2016), where such shadows were stronger in WS events than in WF events. They found that the weaker shadows during WF events stemmed from the buildup and maintenance of prefrontal cold air in the lee, which weakened the mountain waves. This effect is less pronounced over the more axisymmetric Olympics, where impinging air can easily reach the lee side by either ascending the barrier or detouring laterally around it.

5. Numerical setup

Given the uncertainty of our precipitation retrievals and the limited sampling of events, the accuracy and generality of the observational analysis is limited. Although these issues could be addressed by some combination of more observations, more sophisticated retrievals, and/or more event sampling, practical restrictions (e.g., the limited duration of OLYMPEX and inaccessibility of many parts of the Olympics) complicate such efforts. As an alternative, we complement the observations with quasi-idealized numerical simulations, to both evaluate the observed trends and facilitate physical interpretation. The experiments are designed to capture the key differences in orographic precipitation between the different frontal phases while avoiding the many specificities of real cases. While real-case simulations can successfully reproduce the evolution of a given event, they also complicate efforts to quantify specific physical processes of interest. Furthermore, rather than attempting to reproduce the time-evolution of mid-latitude cyclones crossing the Olympics, we consider individual frontal phases in a quasi-steady state.

a. Model configuration

We use the Weather Research and Forecasting (WRF) Advanced Research model (WRF-ARW), version 3.7, an Eulerian split-time-step model with third-order Runge–Kutta time integration on the large time step. Horizontal and vertical advection are fifth and third order, respectively, with positive-definite advection of scalars. The Cartesian domain has a size of 960 km (x) by 480 km (y) by 20 km (z), a horizontal grid spacing of $\Delta_h = 1$ km, and 101 stretched vertical levels. Because unphysical boundary instabilities developed in simulations with open lateral boundaries, periodic boundaries were used instead. The domain size is large enough to prevent gravity waves from fully recirculating

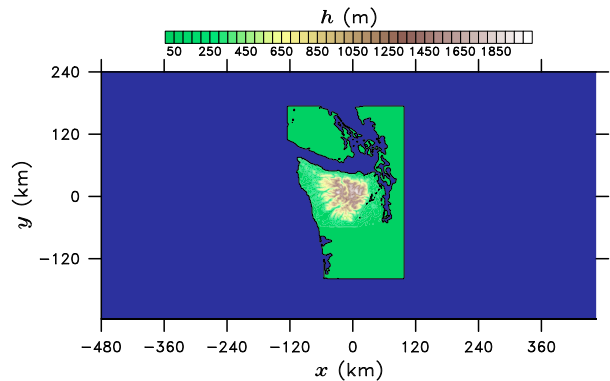


FIG. 8. Grid configuration, land coverage, and terrain height h (filled contours) for the numerical simulations. Water bodies are shown in blue.

through it over a 12-h integration period. Thus, the upstream flow is uncontaminated by such perturbations. The top boundary is rigid with a 8-km-deep sponge layer.

The surface is mostly ocean, with just a strip of the Pacific Northwest in the center (Fig. 8). This configuration eliminates discontinuities at the periodic boundaries while retaining important sea–land contrasts upstream of the Olympics. To focus on the Olympics and avoid sharp terrain gradients at the land edges, the terrain surrounding the Olympics is flattened by creating an irregular pentagon encompassing the Olympics, outside of which the terrain height is set to either 2 m (land) or 0 m (ocean). To limit forcing at poorly resolved scales, and to damp terrain gradients at the polygon edges, a five-point horizontal boxcar smoother is applied to the resulting terrain field. The grid origin is located at the aforementioned Olympics center point.

Physical parameterizations include Thompson microphysics (Thompson et al. 2008) with a maritime cloud-droplet concentration of 100 cm^{-3} , the Yonsei University planetary boundary layer scheme coupled to a surface layer using Monin–Obukhov similarity theory (Hong et al. 2006), horizontal mixing along model surfaces using Smagorinsky closure, and a simple five-layer land surface scheme, where the land use is either water (ocean) or evergreen needleleaf forest (land). The surface is no-slip, with surface heat fluxes used only in the PF simulations (as described below). Radiation is omitted for simplicity.

The initial flows are horizontally homogeneous and defined using a single sounding, which is assumed to be in geostrophic balance. The Coriolis force is applied to perturbations from the initial state using an f -plane approximation ($f = 10^{-4} \text{ s}^{-1}$). The simulations require around 3 h of adjustment to develop a quasi-steady Ekman layer.

b. Initialization

The “control” soundings are designed to capture the key differences between the mean observed soundings

TABLE 4. Upstream parameters and orographic-precipitation metrics for the 18 observed frontal periods.

Event	$ \mathbf{u}_m (\text{m s}^{-1})$	$I(\text{kg m}^{-2} \text{s}^{-1})$	M	CAPE (J kg^{-1})	$r_{\text{up}}(\text{mm h}^{-1})$	DR	DR*	DR _w	DR _w *
WF1	20	419	1.2	0	2.2	0.40	0.09	0.36	0.21
WF2	17	459	1.5	0	3.4	0.21	-0.23	0.19	-0.03
WF3	25	652	1.1	1	1.5	0.23	0.09	0.17	0.10
WF4	30	528	0.9	0	1.4	0.18	0.04	0.15	0.07
WF5	17	450	0.8	0	0.8	0.25	0.13	0.20	0.14
WF6	21	643	1.2	2	2.0	0.21	0.03	0.15	0.06
WF mean	22	525	1.1	1	1.8	0.25	0.03	0.20	0.09
WS1	22	656	0.6	0	1.2	0.31	0.20	0.22	0.16
WS2	22	667	0.5	18	1.0	0.26	0.17	0.18	0.13
WS3	33	737	0.7	0	0.8	0.16	0.09	0.11	0.08
WS4	22	451	0.7	0	1.1	0.18	0.04	0.16	0.09
WS5	23	723	0.9	0	0.7	0.19	0.13	0.13	0.10
WS6	18	605	0.8	0	2.0	0.24	0.05	0.18	0.09
WS mean	23	640	0.7	3	1.1	0.22	0.12	0.16	0.11
PF1	13	178	2.4	116	0.1	0.05	0.02	0.03	0.01
PF2	7	92	3.2	61	0.4	0.22	-0.07	0.18	0.03
PF3	14	185	1.5	33	0.5	0.18	0.00	0.12	0.03
PF4	18	209	1.2	120	0.3	0.24	0.14	0.14	0.09
PF5	8	94	2.7	110	0.1	0.11	0.07	0.10	0.07
PF6	8	78	3.9	2	0.5	0.31	-0.11	0.21	0.00
PF mean	11	139	2.5	74	0.3	0.18	0.01	0.13	0.04

for each frontal phase. They are defined by layers of prescribed Brunt–Väisälä frequency, either dry (N_d^2) or moist (N_m^2), RH, tropopause height z_t and equivalent potential temperature $\theta_{e,t}$, and piecewise-linear wind speed and direction profiles. Parameter settings for the WF, WS, and PF soundings are provided in Table 5. Both the WF and WS soundings are nearly saturated over the depth of the troposphere ($\text{RH}_t = 99\%$), with a tropopause at $z_t = 12$ km. The former uses four layers (subinversion, inversion, free troposphere, and stratosphere), with strong vertical shear and wind veering below the inversion, and the latter is identical except for

using only two thermodynamic layers (troposphere and stratosphere) and no wind veering. Three WF simulations are conducted with varying z_t (3, 2, and 1 km) to represent the gradual descent of the warm front toward the surface. The PF case is distinguished by a smaller RH_t (90%), a weakly stratified boundary layer (up to $z_i = 1$ km), and a low tropopause ($z_t = 8.5$ km).

The idealized soundings in Figs. 9a–c broadly resemble the corresponding three observed soundings in Figs. 4d–f. Moreover, the simulated upstream parameters $|\mathbf{u}_m|$, I , CAPE, and M for the control simulations in Table 6 compare favorably with the mean

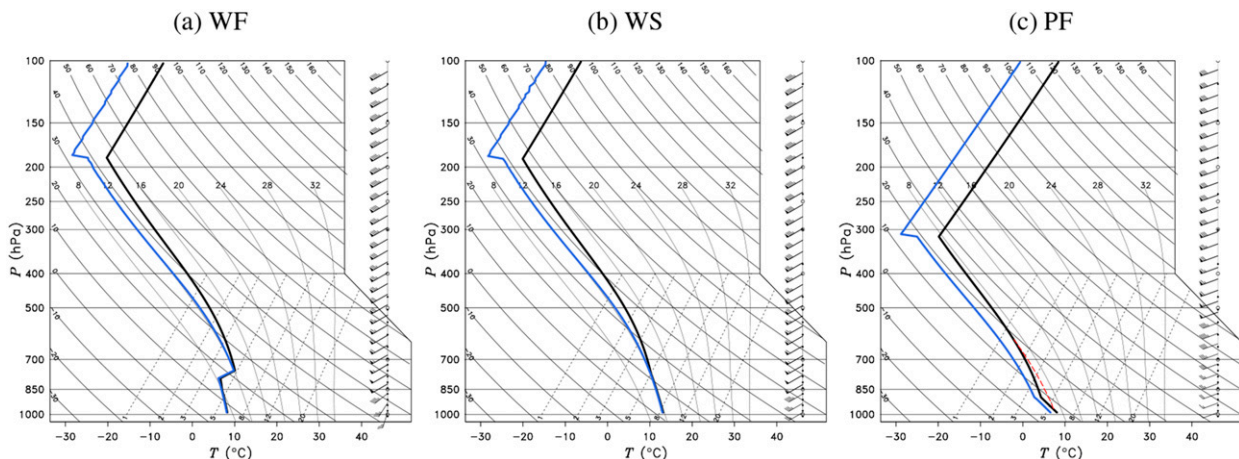


FIG. 9. Idealized skew T – $\log p$ profiles for the (a) WF simulation for $z_i = 2$ km, (b) WS simulation, and (c) PF simulation. The thick black lines are temperature and blue lines are dewpoint. In (c), the red dashed line denotes the temperature profile of an adiabatically lifted parcel originating at the surface, indicating nonzero CAPE.

TABLE 5. Settings for the control soundings. Most symbols are defined in the text, except for the Brunt–Väisälä frequencies in the different layers: subinversion (N_{0-i}^2), inversion (N_i^2), free troposphere (N_t^2), and stratosphere (N_s^2). The parentheticals (m) and (d) denote whether the moist or dry N^2 is used in the layer. Also, z_i is the inversion base (WF) or the boundary layer top (PF), z_u corresponds to an intermediate height for the wind profiles, and \mathbf{u}_0 , \mathbf{u}_1 , and \mathbf{u}_t correspond to the wind vectors at the surface, z_u , and z_t . The wind profiles are linearly interpolated between the specified levels, and the stratospheric winds are given by \mathbf{u}_t .

	WF	WS	PF
z_i (km)	1, 2, 3	—	1
z_t (km)	12	12	8.5
N_{0-i}^2 (10^{-5} s^{-2})	(m) 5	—	(d) 2.5
N_i^2 (10^{-5} s^{-2})	(m) 40	—	—
N_t^2 (10^{-5} s^{-2})	(m) 2.5	(m) 2.5	(m) 0.4
N_s^2 (10^{-5} s^{-2})	(d) 40	(d) 40	(d) 40
RH _{trop}	0.99	0.99	0.9
RH _{strat}	0.5	0.5	0.5
z_u (km)	1.3	1.3	—
$\ \mathbf{u}_0\ $ (m s^{-1}), $\angle \mathbf{u}_0$	10, 190°	10, 240°	7, 250°
$\ \mathbf{u}_u\ $ (m s^{-1}), $\angle \mathbf{u}_u$	25, 240°	25, 240°	—
$\ \mathbf{u}_t\ $ (m s^{-1}), $\angle \mathbf{u}_t$	50, 240°	50, 240°	40, 250°

observed soundings in Table 4, except for slightly smaller $|\mathbf{u}_m|$ and r_{up} , and slightly enhanced M , in the PF sounding.

c. Large-scale forcing

WF and WS events are characterized by large-scale ascent overspreading the Olympics to give widespread precipitation. For simplicity, we assume a scale separation between the synoptic and mesoscale and thus parameterize this forcing as steady and horizontally uniform. This approach, which is commonly used in large-eddy simulations (e.g., Mechem et al. 2010), neglects the complex time and spatial evolution of cyclones, including their tendency to undergo postlandfall decay (e.g., Zishka and Smith 1980). We impose a lifting profile,

$$w_{\text{LS}}(z) = \begin{cases} W_{\text{LS}} \sin\left(\pi \frac{z - z_b}{z_t - z_b}\right) & : z_b \leq z < z_t \\ 0 & : \text{otherwise} \end{cases}, \quad (5)$$

consisting of a half-sine wave between z_b (the layer base) and z_t (the tropopause), with a maximum of W_{LS} at the center. The associated advective tendency on a scalar variable ϕ is then

$$\frac{\partial \phi_{\text{LS}}}{\partial t} = -w_{\text{LS}} \frac{\partial \phi}{\partial z}. \quad (6)$$

These tendencies are added to the potential temperature θ and all water species at each model time step.

Although, in reality, the structure of the large-scale ascent depends on the frontal phase, for simplicity and consistency we fix $z_b = 3.4$ km (the highest inversion top) for all WF and WS experiments. Thus, all parameterized lifting occurs exclusively within the nearly moist neutral warm sector and only modestly changes the temperature or dewpoint profiles within this layer. However, as will be seen, the melting of falling precipitation causes a thin cold layer to develop below the freezing level over the first 3 h of model integration, within which shallow convection develops. The values of W_{LS} that produced acceptable agreement between simulated and observed r_{up} are 0.3 m s^{-1} (WF) and 0.2 m s^{-1} (WS).

Upstream precipitation in PF events is associated not with large-scale ascent, but with cellular convection driven by the flow of polar air over the warmer ocean surface. Thus, we replace the lifting profile with large-scale cooling tendencies over the ocean to represent the replenishment of cold maritime polar air behind the front. The cooling amplitude (5 K day^{-1}) roughly offsets the warming experienced as such air crosses the Pacific midlatitude sea surface temperature (SST) gradient. It is applied over 0–3 km (the layer of largest parcel buoyancy in the observed soundings) and decays linearly to zero at 3.5 km. To sustain upstream moist instability, interactive surface heat fluxes are included with a fixed SST of $T_s + 2$ K, where T_s is the initial sea level air temperature. Over land, the initial skin temperature is set to the air temperature of the corresponding sounding at the same height. Random θ perturbations of amplitude 0.1 K are added to the initial flow to seed convection. For increased sampling of these chaotic convective precipitation fields, an ensemble of five PF simulations is performed, each with different initial perturbations.

6. Model results and discussion

a. Precipitation distributions

The simulated reflectivity of the WF ($z_i = 2$ km), WS, and PF (ensemble member 1) cases at 6 h, after all have reached a quasi-steady state,² shows major differences in precipitation morphology (Fig. 10). Precipitation in the WF simulation is spatially uniform, except for significant OPE upstream of and over the Olympics and a narrow leeside precipitation shadow (Fig. 10a). In contrast, the large-scale precipitation is lighter, and the reflectivity maximum is focused directly over the windward slope in

² During quasi-steady periods, temporal variations of upwind surface flow speed and Olympics-wide precipitation rate were less than $\pm 1.5 \text{ m s}^{-1}$ and 0.2 mm h^{-1} , respectively.

TABLE 6. Upstream parameters and orographic-precipitation metrics for selected numerical simulations. In cases with multiple members (WF.control, WF.noforce, WF.uni, PF.control, and PF.noforce), the values are averaged over all members. Time averages are taken over 3–6 h for all WS and WF simulations and 6–12 h for PF simulations.

Simulation	$ \mathbf{u}_m $ (m s ⁻¹)	I (kg m ⁻² s ⁻¹)	M	CAPE (J kg ⁻¹)	r_{up} (mm h ⁻¹)	DR	DR*	DR _w	DR _w *	PE _w *	FD
WF.control	19	511	1.3	0	1.5	0.21	0.06	0.15	0.08	0.61	0.29
WF.noforce	19	511	1.3	0	0.0	0.01	0.01	0.01	0.01	0.09	0.37
WF.uni	20	522	1.3	0	1.4	0.22	0.06	0.17	0.10	0.75	0.32
WF.1km	20	555	1.5	0	1.4	0.21	0.07	0.15	0.08	0.68	0.25
WF.2km	19	506	1.3	0	1.5	0.20	0.06	0.15	0.08	0.60	0.32
WF.3km	19	471	1.2	0	1.5	0.21	0.05	0.16	0.08	0.54	0.30
WF.2km.uni	20	518	1.3	0	1.4	0.21	0.06	0.17	0.09	0.77	0.35
WF.2km.nm0si	20	528	1.1	0	1.4	0.22	0.07	0.18	0.10	0.61	0.31
WF.2km.noinv	20	595	1.0	0	1.4	0.24	0.10	0.17	0.10	0.56	0.21
WS.control	20	607	0.8	0	1.0	0.20	0.11	0.14	0.10	0.54	0.19
WS.noforce	20	607	0.8	0	0.0	0.06	0.06	0.04	0.04	0.16	0.23
PF.control	8	143	3.0	114	0.2	0.11	0.05	0.06	0.03	0.12	0.38
PF.noforce	8	143	3.0	114	0.0	0.01	0.01	0.01	0.01	0.07	0.49

the WS case (Fig. 10b). The WS precipitation extends to the lee slopes and exhibits a narrower leeside shadow.

Small-scale convective cells induced by melting-layer cooling develop in both the WF and WS simulations but are stronger in the latter. While such cells likely also develop in reality [e.g., Figs. 11–14 of Houze and Medina (2005)], they tend to assume horizontal scales similar to the melting-layer depth (a few hundred meters). The simulated cells, by contrast, scale with the effective grid resolution of 5–10 km. Also, real WF and WS events are characterized by warm advection, which may offset the latent cooling to weaken this convection. Although these cells are thus likely poorly represented, comparison of WS simulations with and without melting-layer cooling suggests that they have minimal impact on the time-averaged precipitation field (not shown).

The PF simulation is characterized by scattered impinging convective cells that widen and multiply over the windward slopes (Fig. 10c). Precipitation mostly vanishes downwind, except for quasi-stationary longitudinal bands that may stem from leeside flow convergence (e.g., Mass 1981). Although the upstream M is much larger than that in the WF cases (Table 6), the flow undergoes less near-surface deflection around the barrier. We hypothesize that terrain-forced saturation over the lower windward slope decreases the effective stability and, hence, M , allowing more fluid to ascend the barrier than might otherwise be expected (e.g., Jang 2003).

Vertical cross sections of reflectivity and instantaneous streamlines along the mean subcrest wind direction show that mountain waves develop as statically stable impinging flow is displaced upward by the upstream blocked zone and the terrain itself (Fig. 10d). The upstream tilt of these waves gives rise to a broad upstream extension of clouds and precipitation. A bright

band of enhanced reflectivity is apparent in the melting layer ($z \approx 1$ km), which descends to the surface over the windward slope and reforms in the lee at a higher elevation. The former arises from forced lifting of stably stratified flow (Minder et al. 2011), and the latter stems from the warming of the mountain wake due to windward latent-heat release and lee-wave breaking.

Mountain waves also develop in the WS case, but the weak tropospheric moist stability does not induce obvious upstream tilting (Fig. 10e). Instead, vertically aligned updrafts extend deep into the troposphere to focus the OPE over the high terrain, with some lee spillover. In the PF case, convective cells dominate the streamline displacements in the conditionally unstable 0–3-km layer (Fig. 10f). These coexist with small-amplitude mountain waves that propagate through the largely statically stable flow (except in saturated areas). The combination of coastal frictional convergence, partial upstream blocking of the impinging flow, and upstream-tilted mountain waves enhances the concentration of convective cells between the coastline and the mountain crest.

Mean simulated precipitation rates are calculated by averaging over quasi-steady periods: 3–6 h in WF/WS and 6–12 h in PF (all subsequent time averaging uses these same respective intervals). We then obtain model composites by averaging over all simulations of a given frontal type: three cases of different inversion heights for WF, one case for WS, and five ensemble members for PF. The resulting precipitation rates from these “control” simulations in Fig. 11 show similar sensitivities to frontal phase as the corresponding observational retrievals in Fig. 7: (i) the WF case forms a broad OPE region extending well upstream (to the south and west) of the Olympics, (ii) the WS case exhibits a stronger OPE, focused directly over the Olympics, and (iii) the

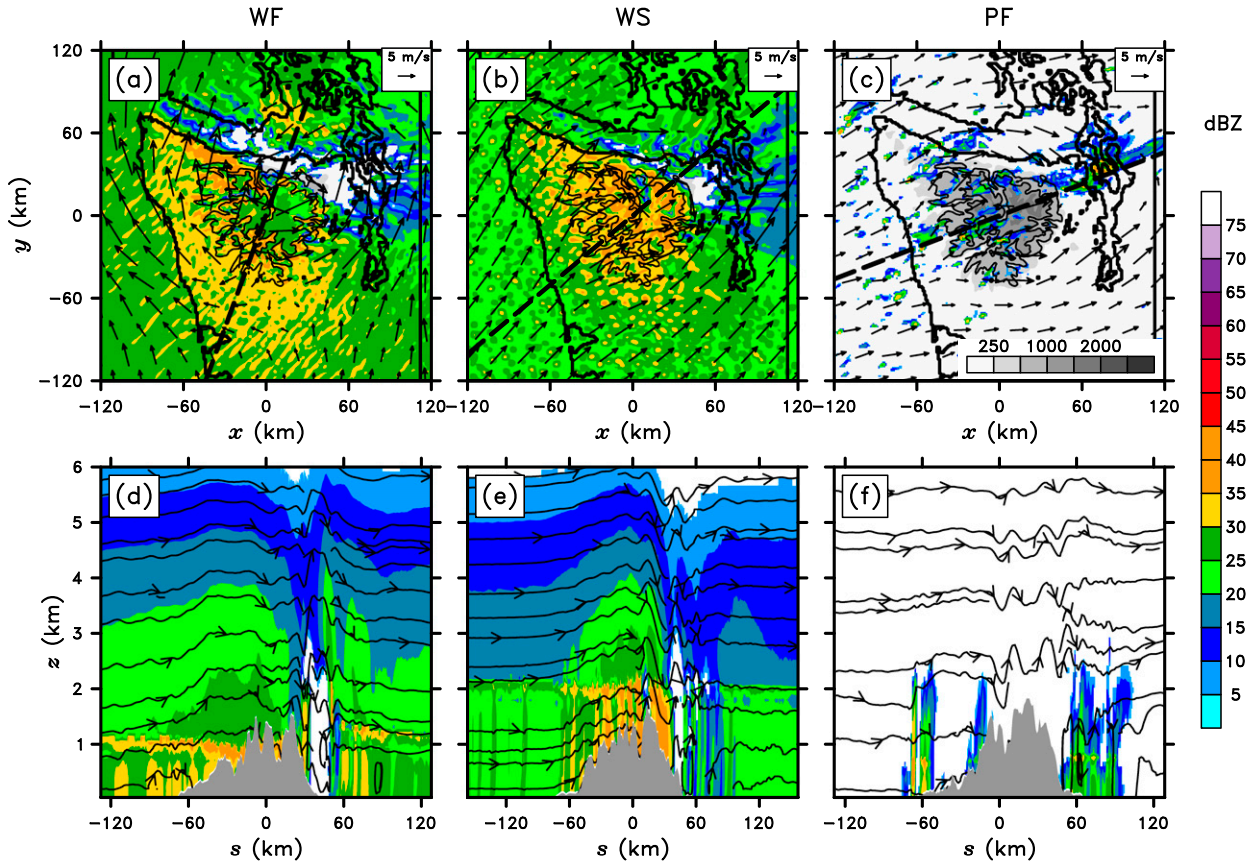


FIG. 10. Simulated reflectivity and winds in the control simulations. The top panels show snapshots of lowest-model-level wind vectors and reflectivity (color fill), along with terrain height (grayscale, in m, with 1-km contour overlaid in black) at 6 h of the (a) WF.control ($z_t = 2$ km), (b) WS, and (c) PF.control (member 1) simulations. (d)–(f) Vertical cross sections (along the dashed lines shown in corresponding top panels), roughly parallel to the mean subcrest wind direction, of reflectivity (color fill) and streamlines from the same simulations. The abscissa s shows distance along the cross section from left to right.

PF case develops light precipitation with a weak OPE over the lower windward slopes.

The precipitation distributions in Fig. 11 differ from those obtained in a comparable modeling study of Picard and Mass (2017), who systematically examined the sensitivity of Olympics precipitation to impinging wind direction and surrounding terrain. Whereas their Olympics precipitation maxima formed well upstream of the crest, ours tend to develop farther inland. These differences may stem from differences in model initial configurations, including their use of weaker low-level winds and their omission of large-scale forcing. Moreover, while Picard and Mass (2017) found a strong sensitivity of Olympics precipitation to the presence of surrounding terrain, we did not: results from an additional set of simulations that included the surrounding topography differed minimally from those in Fig. 11 (not shown).

b. Quantitative analysis

The combination of surface friction and upstream blocking causes the simulated \mathbf{u}_m and I at the model

NPOL site to decrease relative to the corresponding initial values in Table 6. This reduction is maximized in the WF simulations (10%–13%) due to their strongly blocked near-surface flows and is weaker in the PF (6%) and WS (8%) simulations, which reinforces that the observed coastal soundings in Table 3 do not fully represent the impinging marine flow.

Simulated orographic-precipitation metrics, calculated identically to those in the corresponding observational analysis in Table 4, are presented in Table 6. Although the simulated DR , DR^* , DR_w , and DR_w^* differ variously with the observations, they obey similar trends with respect to frontal phase: DR and DR_w are the largest in WF (by a small margin over WS) and the smallest in PF, and DR^* and DR_w^* are the largest in WS and smallest in PF. Thus, as in the observations, the total orographic precipitation (including both the larger-scale and the orographic enhancement) is the largest for WF, but the enhancement itself (or OPE) is maximized for WS.

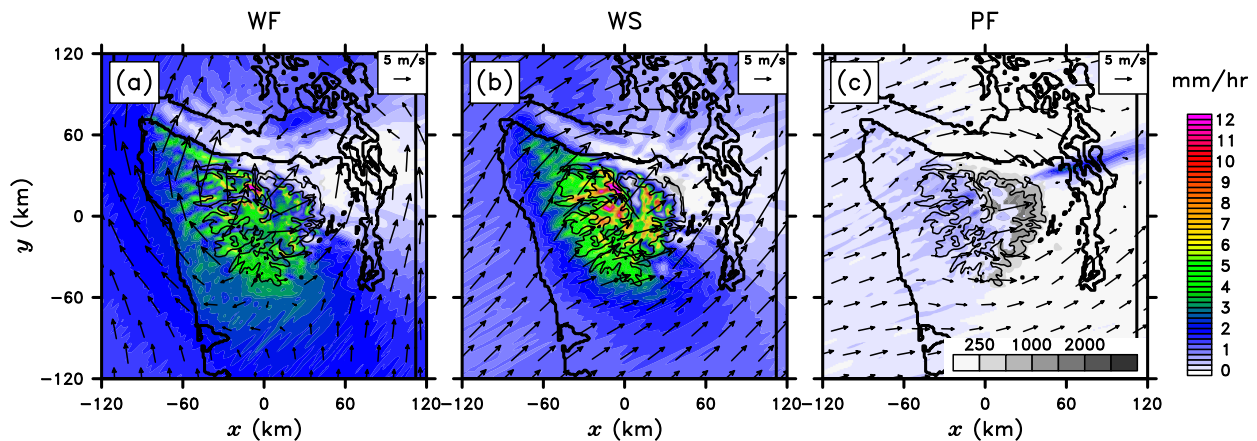


FIG. 11. Time-averaged surface r (color fill), lowest-model-level wind vectors, terrain height (grayscale, in m, with 1000-m contour overlaid in black) of the (a) WF.control, (b) WS.control, and (c) PF.control simulations. Time averages are taken over 3–6 h for WS and WF simulations and 6–12 h for PF simulations.

Because of shortcomings of both the simulations and the retrievals, the two should not be expected to agree perfectly. Nevertheless, the above comparison suggests that the former captures most of the key trends seen in the latter. Some notable discrepancies also exist, like an apparent overprediction in simulated precipitation over the northern Olympics ($|x| < 20$, $0 \leq y \leq 30$ km). This issue may relate to the lack of gauge data and the relatively high radar beam in this region (Figs. 1a, 3a), as well as the failure of our model soundings to capture the full diversity or complexity of real upstream flows. The simulated precipitation also lacks the southward extension and the secondary maximum over the Cascades seen in the observations. While these discrepancies stem in part from our flattening of these terrain features, the former also relates to a nonorographic effect: a transient but intense squall line developed to the south of the Olympics during PF2, which locally increased the composite precipitation (not shown).

Table 6 also presents the windward OPE efficiency (PE_w^*), defined as the ratio of the time-averaged windward precipitation (P_w^*) to condensation (C_w^*) enhancements relative to the corresponding upstream values. This evaluation is restricted to the windward side to avoid complications associated with leeside evaporation. A $200 \text{ km} \times 200 \text{ km}$ horizontal box is defined with its downwind edge centered at the grid origin and its upstream edge facing the windward side defined by \mathbf{u}_m . The averaged precipitation and vertically integrated condensation rates over this box, minus the corresponding upstream values (averaged over the region extending from the upstream box edge to the upstream domain boundary), give PE_w^* . The resulting values are large ($>50\%$) in both the WF.control and WS.control cases, but much smaller ($<20\%$) in the PF.control

simulation. The mechanisms regulating these variations in PE_w^* are discussed in section 6c.

To quantify the degree of upstream blocking, we compute the fraction of impinging subcrest flow that deflects around the barrier [termed FD for flow deflection, after Reinecke and Durran (2008)]. A rectangular control volume is defined with an along-flow length of 120 km, a width of 80 km to encompass the highest peaks, and a depth equal to the simulated terrain maximum (1961 m), with its downwind edge centered at the origin and its upstream edge facing the windward direction defined by \mathbf{u}_m (see Fig. 12 for an example). FD is evaluated as

$$FD = -\frac{F_U}{F_L + F_R}, \quad (7)$$

where F_U , F_L , and F_R are the respective mass fluxes into the upstream and two lateral edges.

Consistent with the corresponding variations in M , FD is a maximum in PF.control (0.38), smaller in WF.control (0.29), and a minimum in WS.control (0.19) (Table 6). In the WF case with veering low-level winds, FD may underestimate the true flow deflection near the surface because the southerly impinging flow is not aligned with the corresponding control volume. However, FD increases only modestly in three WF simulations that, instead of using a veered initial wind profile, use the same unidirectional wind profiles as the WS simulation (WF.uni).

c. Sensitivity to large-scale precipitation

Figure 13 compares the OPEs (i.e., $r - r_{\text{up}}$) for two sets of simulations: the control cases and corresponding simulations with zero large-scale forcing (i.e., $W_{\text{LS}} = 0$

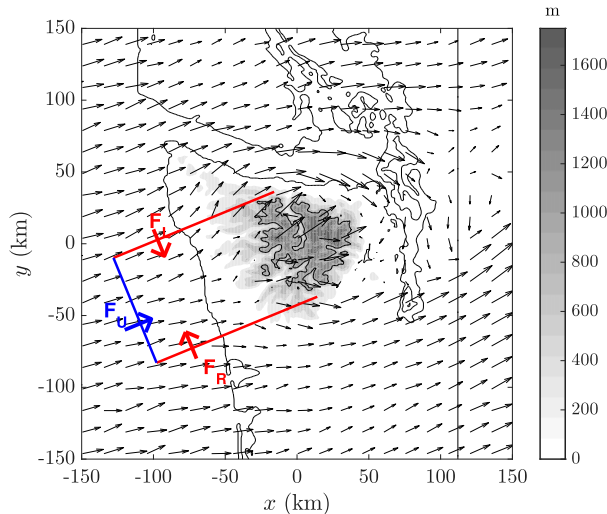


FIG. 12. Lateral boundaries of the control volume used for the FD calculation (here, oriented for the PF simulations, overlaid on terrain in grayscale and lowest-model-level winds at 9 h), showing the relevant flux terms in (7).

for WF/WS and zero large-scale cooling and surface heat fluxes for PF). These experiments are named WF.noforce, WS.noforce, and PF.noforce. Compared to WF.control, both the extent and amplitude of the OPE decrease drastically in WF.noforce (Figs. 13a,d), as do all DR metrics (Table 6). Part of this reduction stems from an effective increase in the flow stability and hence, M , due to an increased prevalence of unsaturated flow, which causes FD to increase by $\sim 28\%$. Another part is owing to reduced PE_w^* , which decreases around fivefold. This sharply reduced PE_w^* and hence, OPE, is primarily owing to the absence of larger-scale seeder clouds.

In the WS.noforce case, the OPE again weakens and contracts to the highest terrain (Figs. 13b,e), leading to major reductions in all DR metrics and in PE_w^* (Table 6). However, the drop-off in these parameters from the control case is much less than that in the WF simulations: rather than decreasing by around a factor of 5, they only decrease by a factor of 2–3. This moderation stems from the weaker low-level static stability of the WS sounding, which limits upstream blocking and flow deflection despite the absence of widespread saturation. As a result, terrain-forced ascent remains strong, and deep mountain waves (not shown) still focus precipitation over the windward slope. In the absence of cloud seeding, the associated clouds are simply less efficient at producing precipitation that reaches the windward slope.

Precipitation also decreases in the PF.noforce case (Figs. 13c,f), where only a weak and narrow band forms

over the windward slope ($x \approx -30$, $y \approx -10$ km). This weakening stems from deceleration and increased deflection of low-level flow around the barrier (manifested as a 30% increase in FD), driven by the absence of surface heating and associated vertical mixing of momentum. Although this enhanced blocking is limited to the 0–500-m layer, this layer contains all of the CAPE, and thus, the orographic convection is disproportionately suppressed. Also, PE_w^* decreases slightly, likely due to a slight reduction in cumulus cloud depth (not shown).

To systematically quantify the sensitivity of OPEs to r_{up} , we conduct sets of WF and WS simulations where W_{LS} in (5) is progressively varied. To limit expense, these experiments use $\Delta_t = 2$ km, which does not affect the basic model sensitivities (not shown). Nine values of W_{LS} are considered: 0, 0.01, 0.02, 0.03, 0.05, 0.1, 0.2, 0.3, and 0.5 m s^{-1} , encompassing the control values for both the WF and WS cases. Because synoptic forcing is limited to the midtroposphere ($z > 3.4$ km), the W_{LS} values required to produce a meteorologically relevant range of r_{up} exceed the strength of typical synoptic-scale updrafts ($\sim 0.2 \text{ m s}^{-1}$).

Not surprisingly, as W_{LS} (and hence, r_{up}) increases, so do DR and DR_w (Fig. 14), which both effectively include r_{up} . However, focusing on just the OPE, DR_w^* increases rapidly as r_{up} is increased from 0 to 0.5 mm h^{-1} , but then remains insensitive to further increases in r_{up} . Thus, as in Richard et al. (1987), only modest large-scale precipitation is required to fully realize the seeder–feeder effect. As a result, DR^* increases with r_{up} only for small r_{up} , then decreases at larger r_{up} due to progressively increasing leeside evaporation. This decrease is stronger in the WF simulations because (i) their intense leeside downdrafts readily evaporate larger-scale precipitation, and (ii) the larger spillover in the WS case (e.g., Fig. 10e) humidifies the leeside flow.

d. The upstream shift in warm-frontal precipitation

Both the observations and simulations suggest that OPEs in the WF cases are weaker and extend farther upstream than those in the WS cases (Figs. 7, 11–13; Tables 4, 6). These differences cannot be attributed to r_{up} or PE_w^* because, as just discussed, the former has little impact for $r_{up} > 0.5 \text{ mm h}^{-1}$ (as in WF.control and WS.control), and the latter varies minimally between the two simulation types. Rather, they are linked to differences in flow dynamics, namely, stronger upstream flow blocking and lateral deflection in WF cases. Because the upstream flows of these cases differ mainly in their low-level static stabilities, particularly the presence of the stable inversion and subinversion layers in WF cases, we seek to isolate the

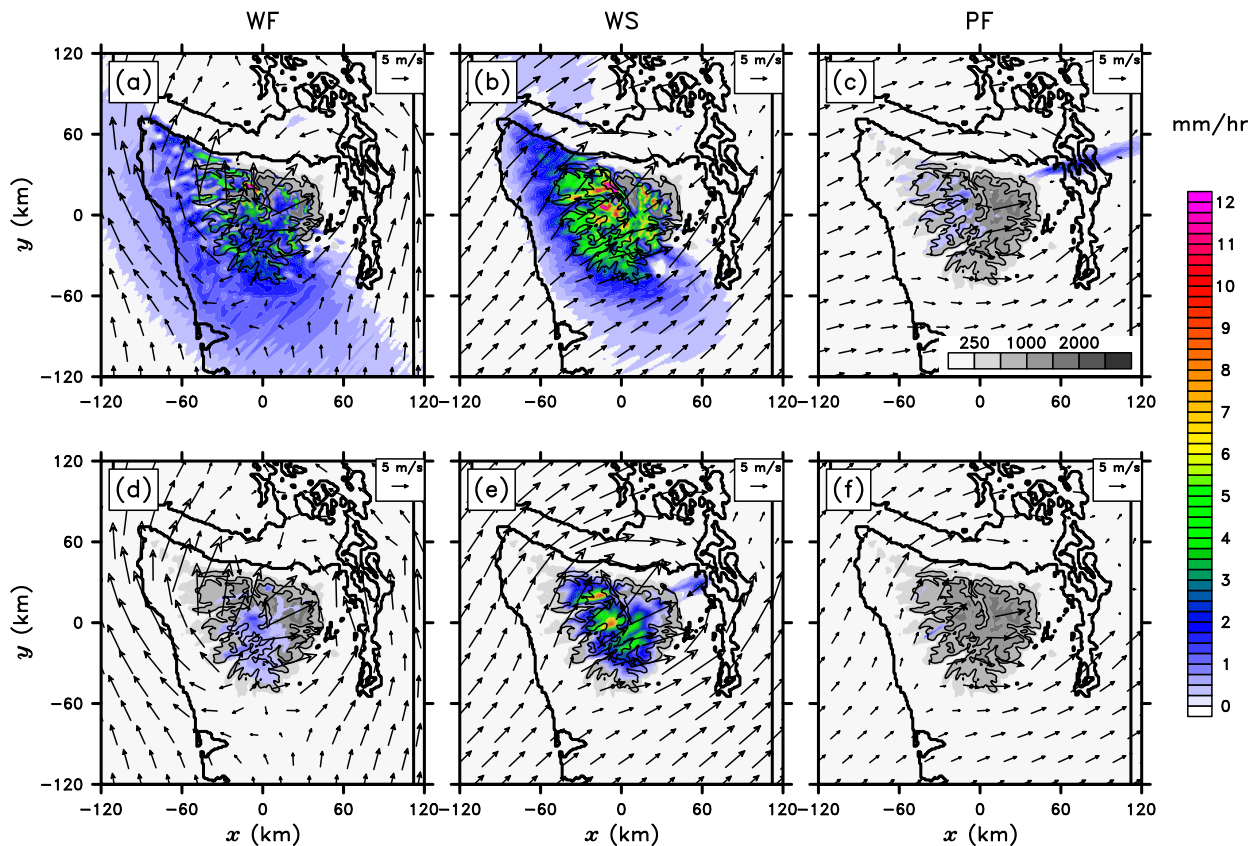


FIG. 13. Time-averaged surface precipitation rate enhancement relative to the mean upstream value (color fill; only positive values shown), lowest-model-level wind vectors, terrain height (grayscale, in m, with 1-km contour overlaid in black) of the (a) WF.control, (b) WS.control, (c) PF.control, (d) WF.noforce, (e) WS.noforce, and (f) PF.noforce simulations. Time averages are taken over 3–6 h for WS and WF simulations and 6–12 h for PF simulations.

contributions of each layer to the differences between the WF and WS results.

We compare four simulations, the WF.uni case with $z_i = 2$ km (WF.2km.uni), WS, and two simulations that are identical to WF.2km.uni, except for equating N_m in either the inversion layer (WF.2km.noinv) or the subinversion layer (in WF.2km.nm0si) to the smaller warm sector value ($N_m^2 = 2.5 \times 10^{-5} \text{ s}^{-2}$). The unidirectional winds sidestep the difficulties of calculating FD in layers with strong directional shear. As shown in Table 6, FD in WF.2km.noinv (0.21) lies closer to that in WS (0.19), while FD in WF.2km.nm0si (0.31) lies closer to that in WF.2km.uni (0.32). Thus, the inversion contributes more to the stronger blocking in the WF simulations than does the subinversion layer. Given that the potential for blocking is often diagnosed based on just the subcrest conditions (e.g., Reinecke and Durran 2008), and that this inversion nominally lies above crest level, this finding may come as a surprise. However, it is consistent with the hydrostatic theory of Smith (1989) and Kirshbaum (2017), where vertical displacements over

the entire fluid column contribute to the adverse pressure gradients that decelerate the impinging flow.

7. Summary and conclusions

This study has synthesized observations and numerical simulations to interpret the synoptic controls on orographic precipitation over the Olympics Mountains of Washington State during the OLYMPEX field campaign in winter 2015/16. The observational analysis included routine and special measurements within 18 well-observed, manually classified frontal periods: six ahead of warm fronts (WF), six within warm sectors (WS), and six behind cold fronts (postfrontal, or PF). Complementary quasi-idealized simulations, constrained by relevant OLYMPEX observations, were conducted to aid physical interpretation.

Both observational precipitation retrievals for the 18 frontal periods and the simulations revealed that while the upstream extent and magnitude of time-averaged orographic precipitation were the largest in WF events

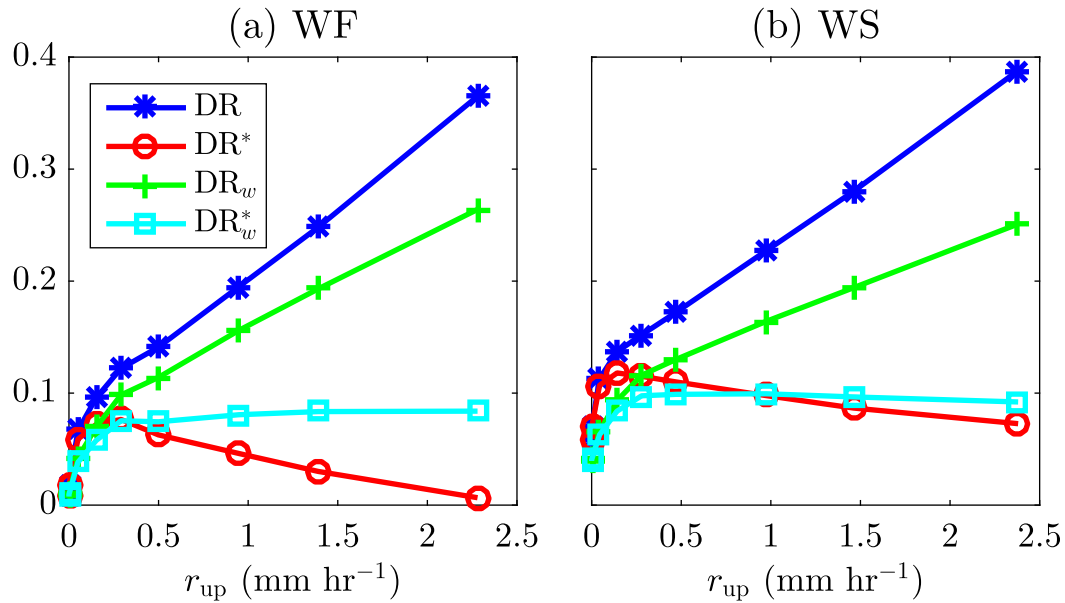


FIG. 14. Sensitivity of various drying ratio metrics to r_{up} for the (a) WF and (b) WS simulations.

(broadly $5\text{--}10\text{ mm h}^{-1}$), the orographic precipitation enhancement (OPE) was the largest, and focused largely over the high windward slopes, in the WS events. Whereas the precipitation in WF/WS events was largely deep and stratiform (with some embedded convection), it was shallow and convective in the PF events, with impinging cells or bands forming over the Pacific Ocean and becoming larger and more numerous near the upstream foot of the Olympics. Time-averaged precipitation in the PF events was generally light ($<2\text{ mm h}^{-1}$), with modest OPEs over the lower windward slopes.

Most of the differences in orographic precipitation distributions among the different frontal types can be explained on the basis of their upstream conditions. The magnitude of the orographic precipitation largely depended on the upstream precipitation rate and the impinging horizontal moisture flux, both of which were much larger in WF/WS events than in PF events. Relative to the WS events, the upstream shift in WF precipitation stemmed largely from a more stable lower troposphere, which gave rise to increased near-surface flow blocking and upstream convergence, lateral deflection around the barrier, and upstream-tilted mountain waves. Warm-frontal inversion layers, even those nominally lying just above crest level, played a larger role in the upstream blocking than did the subinversion stability, at least for the parameter space under consideration. Unlike the saturated WF/WS impinging flows, the upstream flows in the PF events were nominally unsaturated, with consequently larger static stability and

nondimensional mountain heights M . Although forced saturation over the windward slopes reduced the effective static stability and M , the PF cases still experienced the largest subcrest flow deflection around the barrier.

Due mainly to their seeding by larger-scale precipitation, the orographic clouds in both WF and WS events were highly efficient at enhancing precipitation over the windward slopes. When the simulated larger-scale precipitation was eliminated, the precipitation efficiency of these clouds decreased dramatically, as did the upstream extent of the OPE. However, similar to Richard et al. (1987), this increased precipitation efficiency stemming from the seeder–feeder process did not require intense precipitation from the “seeder” (i.e., larger scale) cloud: background precipitation rates of only 0.5 mm h^{-1} sufficed to fully realize this enhancement.

Although the results obtained herein provide useful insights into Olympics precipitation, their accuracy is limited by numerous uncertainties and simplifications. Limitations of the observational precipitation retrievals include (i) extensive radar beam blockage over the high terrain, (ii) the use of a fixed $Z-r$ relation for mixed-phase precipitation, (iii) the neglect of dual-polarization information, which can improve radar precipitation estimates (e.g., Seo et al. 2015), (iv) the sparsity of the observed gauge network over the Olympics, and (v) gauge representativity errors. The simulations are also limited by (i) the parameterization of large-scale forcing as steady and horizontally uniform, (ii) the simplistic representation of upstream thermodynamic and wind profiles, and (iii) uncertainties in model subgrid

parameterizations, such as cloud microphysics and boundary layer turbulence. Because of these limitations, retrievals using denser gauge networks and more sophisticated algorithms, analyses of a larger collection of observed events (including occluded fronts), and ensembles of more realistic simulations that consider uncertainties in physical parameterizations and initial conditions are recommended for future work.

Acknowledgments. We are grateful to the OLYMPEX team at the University of Washington, specifically Bob Houze, Lynn McMurdie, Joe Zagrodnik, and Stacy Brodzik, for sharing valuable data and advising on its usage. We also thank Frédéric Fabry, John Gyakum, Dave Hudak, and Dave Schultz for useful insights during the course of this study. Funding from the Marine Environmental Observation Prediction and Response (MEOPAR) network Grant EC1-DK-MCG and by the Natural Science and Engineering Research Council Grant NSERC/RGPIN 418372-12 is acknowledged. Numerical simulations were performed on the Guillimin supercomputer at McGill University, under the auspices of Calcul Québec and Compute Canada. We are grateful for insightful comments from editor Hugh Morrison and three anonymous reviewers.

APPENDIX

2D-VAR Methodology

As in B13, we define \mathbf{x} as the (unknown) state vector of length $S_x = N_x N_y$, where N_x and N_y are the number of grid points in the west–east and south–north directions, and \mathbf{y} is the vector of S_y gauge observations. These variables are related by

$$\mathbf{x} = \mathbf{x}_b + \boldsymbol{\epsilon}, \quad (\text{A1})$$

$$\mathbf{y} = h(\mathbf{x}) + \boldsymbol{\eta}, \quad (\text{A2})$$

where \mathbf{x}_b is the background state vector, h is the nonlinear forward model, and $\boldsymbol{\epsilon}$ and $\boldsymbol{\eta}$ are the error vectors of the background state and the observation.

We set $\mathbf{x} = \ln \mathbf{r}$, $\mathbf{x}_b = \ln \mathbf{r}_{\text{MFB}}$, and $\mathbf{y} = \mathbf{r}_g$, where \mathbf{r} is the (unknown) precipitation rate vector and \mathbf{r}_g is the gauge observation vector. The logarithmic form of \mathbf{x} and \mathbf{x}_b prevents unphysical negative rain rates. Maximizing the probability of \mathbf{x} given \mathbf{y} is equivalent to minimizing the cost function:

$$J(\mathbf{x}) = (\mathbf{x} - \mathbf{x}_b)^T \mathbf{B}^{-1} (\mathbf{x} - \mathbf{x}_b) + [\mathbf{y} - h(\mathbf{x})]^T \mathbf{R}^{-1} [\mathbf{y} - h(\mathbf{x})], \quad (\text{A3})$$

where \mathbf{B} and \mathbf{R} are the background and observation error covariance matrices. These matrices control the

weighting of the background and observations and the spreading of observational information in the estimate of \mathbf{x} . A Gauss–Newton iterative method is used to minimize a linearized version of (A3) and converge to the optimal \mathbf{x} (see B13 for details).

To parameterize the observation error covariance matrix \mathbf{R} , we assume that the errors from different precipitation gauges are uncorrelated (as in B13), and hence, the matrix is diagonal. We further assume that over each hourly assimilation period, the gauge quantization error is negligible relative to the “representativity” error associated with the use of a single point gauge measurement to represent a $2 \text{ km} \times 2 \text{ km}$ grid box. This error is estimated by finding all pairs of gauges located within 2 km of each other, 15 of which exist in total in the plot area of Fig. 1a. As representativity errors generally increase over higher terrain, we subdivide these pairs into two sets: those located over relatively flat ground (terrain heights less than 500 m) and those over higher ground. Of the 15 pairs, 14 fell into the first set, with only one, located over the southern slopes of Mt. Rainier near 46.8°N , -121.5°E , and terrain heights of 1564 and 1646 m (Fig. 1a), falling into the second.

Assuming that the gauge error is the same for each pair of gauges, the associated representativity error on $\ln r_g$ is computed following B13 as

$$\Delta \ln r_g = \sqrt{\frac{(\ln r_{g_1} - \ln r_{g_2})^2}{2}}, \quad (\text{A4})$$

where r_{g_1} and r_{g_2} are hourly precipitation rates from the two gauges. The averaging operation in (A4) considers the collective set of hourly measurements for all WF and WS periods in Table 1. The resulting values of $\Delta \ln r_g$ are 0.32 for the low-terrain sites and 0.89 for the high-terrain sites, hence $\Delta r_g = 0.32 r_g$ and $0.89 r_g$, respectively. The \mathbf{R} matrix is then filled by applying the latter over all of the high Olympics regions defined in Fig. 3b (KLGX2, KATX2.1, and UPPER) and the former elsewhere.

Parameterization of the background error covariance matrix \mathbf{B} requires estimation of the error in the “background” MFB analysis ($\Delta \ln r_{\text{MFB}}$). Assuming that this error is uncorrelated with the rain gauge representativity error, B13 obtained

$$\Delta \ln r_{\text{MFB}} = \sqrt{(\ln r_g - \ln r_{\text{MFB}})^2 - (\Delta \ln r_g)^2}, \quad (\text{A5})$$

where the averaging operation in (A4) is performed for all WF and WS periods over all hourly measurements. This calculation is performed separately over the

low-terrain and high-terrain areas described above, giving $\Delta \ln r_{\text{MFB}} = 1.15$ and 1.54 , respectively.

The above values of $\Delta \ln r_{\text{MFB}}$ comprise the diagonal entries of \mathbf{B} , or \mathbf{B}_{ii} . Because the MFB analysis is strongly constrained by radar data, its errors are correlated in space (Berenguer and Zawadzki 2008). This correlation is accounted for by prescribing off-diagonal entries as

$$\mathbf{B}_{ij} = \mathbf{B}_{ii} \exp\left(-\frac{d_{ij}}{d_0}\right), \quad (\text{A6})$$

where $d_0 = 5$ km. This value of d_0 is larger than that used by B13 (1.5 km), which was obtained through a rigorous analysis of radar and gauge data. Rather than performing a similar analysis herein, which would be complicated by variable error correlations in space due to terrain blocking effects (an issue that was not present in B13), we simply assumed a larger value.

REFERENCES

- Berenguer, M., and I. Zawadzki, 2008: A study of the error covariance matrix of radar rainfall estimates in stratiform rain. *Wea. Forecasting*, **23**, 1085–1101, <https://doi.org/10.1175/2008WAF2222134.1>.
- Bergeron, T., 1965: On the low-level redistribution of atmospheric water caused by orography. *Proc. Int. Conf. on Cloud Physics*, Tokyo, Japan, Amer. Meteor. Soc., 96–100.
- Bianchi, B., P. J. van Leeuwen, R. J. Hogan, and A. Berne, 2013: A variational approach to retrieve rain rate by combining information from rain gauges, radars, and microwave links. *J. Hydrometeorol.*, **14**, 1897–1909, <https://doi.org/10.1175/JHM-D-12-094.1>.
- Bluestein, H. B., and P. C. Banacos, 2002: The vertical profile of wind and temperature in cyclones and anticyclones over the eastern two-thirds of the United States: A climatology. *Mon. Wea. Rev.*, **130**, 477–506, [https://doi.org/10.1175/1520-0493\(2002\)130<0477:TVPOWA>2.0.CO;2](https://doi.org/10.1175/1520-0493(2002)130<0477:TVPOWA>2.0.CO;2).
- Cannon, D. J., D. J. Kirshbaum, and S. L. Gray, 2012: Under what conditions does embedded convection enhance orographic precipitation? *Quart. J. Roy. Meteor. Soc.*, **138**, 391–406, <https://doi.org/10.1002/qj.926>.
- Cao, Q., T. H. Painter, W. R. Currier, J. D. Lundquist, and D. P. Lettenmaier, 2018: Estimation of precipitation over the OLYMPEX domain during winter 2015/16. *J. Hydrometeorol.*, **19**, 143–160, <https://doi.org/10.1175/JHM-D-17-0076.1>.
- Chumchean, S., A. Sharma, and A. Seed, 2006: An integrated approach to error correction for real-time radar-rainfall estimation. *J. Atmos. Oceanic Technol.*, **23**, 67–79, <https://doi.org/10.1175/JTECH1832.1>.
- Colle, B. A., and C. F. Mass, 2000: The 5–9 February 1996 flooding event over the Pacific Northwest: Sensitivity studies and evaluation of the MM5 precipitation forecasts. *Mon. Wea. Rev.*, **128**, 593–617, [https://doi.org/10.1175/1520-0493\(2000\)128<0593:TFFEOT>2.0.CO;2](https://doi.org/10.1175/1520-0493(2000)128<0593:TFFEOT>2.0.CO;2).
- , —, and K. J. Westrick, 2000a: MM5 precipitation verification over the Pacific Northwest during the 1997–99 cool seasons. *Wea. Forecasting*, **15**, 730–744, [https://doi.org/10.1175/1520-0434\(2000\)015<0730:MPVOTP>2.0.CO;2](https://doi.org/10.1175/1520-0434(2000)015<0730:MPVOTP>2.0.CO;2).
- , —, and K. J. Westrick, 2000b: MM5 precipitation verification over the Pacific Northwest during the 1997–99 warm seasons. *Wea. Forecasting*, **15**, 745–758, [https://doi.org/10.1175/1520-0434\(2000\)015<0745:MPVOTP>2.0.CO;2](https://doi.org/10.1175/1520-0434(2000)015<0745:MPVOTP>2.0.CO;2).
- Cookson-Hills, P., D. J. Kirshbaum, M. Surcel, J. G. Doyle, L. Fillion, D. Jacques, and S.-J. Baek, 2017: Verification of 24-h quantitative precipitation forecasts over the Pacific Northwest from a high-resolution ensemble Kalman filter system. *Wea. Forecasting*, **32**, 1185–1208, <https://doi.org/10.1175/WAF-D-16-0180.1>.
- Daly, C., M. Halbleib, J. I. Smith, W. P. Gibson, M. K. Doggett, G. H. Taylor, J. Curtis, and P. P. Pasteris, 2008: Physio-graphically sensitive mapping of climatological temperature and precipitation across the conterminous United States. *Int. J. Climatol.*, **28**, 2031–2064, <https://doi.org/10.1002/joc.1688>.
- Durran, D. R., and J. B. Klemp, 1982: On the effects of moisture on the Brunt–Väisälä frequency. *J. Atmos. Sci.*, **39**, 2152–2158, [https://doi.org/10.1175/1520-0469\(1982\)039<2152:OTEOMO>2.0.CO;2](https://doi.org/10.1175/1520-0469(1982)039<2152:OTEOMO>2.0.CO;2).
- Hobbs, P. V., 1975: The nature of winter clouds and precipitation in the Cascade Mountains and their modification by artificial seeding. Part I: Natural conditions. *J. Appl. Meteor.*, **14**, 783–804, [https://doi.org/10.1175/1520-0450\(1975\)014<0783:TNOWCA>2.0.CO;2](https://doi.org/10.1175/1520-0450(1975)014<0783:TNOWCA>2.0.CO;2).
- Hong, S.-Y., Y. Noh, and J. Dudhia, 2006: A new vertical diffusion package with an explicit treatment of entrainment processes. *Mon. Wea. Rev.*, **134**, 2318–2341, <https://doi.org/10.1175/MWR3199.1>.
- Houze, R. A., and S. Medina, 2005: Turbulence as a mechanism for orographic precipitation enhancement. *J. Atmos. Sci.*, **62**, 3599–3623, <https://doi.org/10.1175/JAS3555.1>.
- , and Coauthors, 2017: The Olympic Mountains Experiment (OLYMPEX). *Bull. Amer. Meteor. Soc.*, **98**, 2167–2188, <https://doi.org/10.1175/BAMS-D-16-0182.1>.
- Jiang, Q., 2003: Moist dynamics and orographic precipitation. *Tellus*, **55A**, 301–316, <https://doi.org/10.1034/j.1600-0870.2003.00025.x>.
- Kingsmill, D. E., P. J. Neiman, F. M. Ralph, and A. B. White, 2006: Synoptic and topographic variability of Northern California precipitation characteristics in landfalling winter storms observed during CALJET. *Mon. Wea. Rev.*, **134**, 2072–2094, <https://doi.org/10.1175/MWR3166.1>.
- Kirshbaum, D. J., 2017: On upstream blocking over heated mountain ridges. *Quart. J. Roy. Meteor. Soc.*, **143**, 53–68, <https://doi.org/10.1002/qj.2945>.
- , and R. B. Smith, 2008: Temperature and moist-stability effects on midlatitude orographic precipitation. *Quart. J. Roy. Meteor. Soc.*, **134**, 1183–1199, <https://doi.org/10.1002/qj.274>.
- , and A. L. M. Grant, 2012: Invigoration of cumulus cloud fields by mesoscale ascent. *Quart. J. Roy. Meteor. Soc.*, **138**, 2136–2150, <https://doi.org/10.1002/qj.1954>.
- Langston, C., and J. Zhang, 2004: An automated algorithm for radar beam occultation. *11th Conf. on Aviation, Range, and Aerospace, and 22nd Conf. on Severe Local Storms*, Hyannis, MA, Amer. Meteor. Soc., P5.16, https://ams.confex.com/ams/11aram22sls/techprogram/paper_81932.htm.
- Lewis, H. W., and D. L. Harrison, 2007: Assessment of radar data quality in upland catchments. *Meteor. Appl.*, **14**, 441–454, <https://doi.org/10.1002/met.43>.
- Lin, Y., and K. E. Mitchell, 2005: The NCEP stage II/IV hourly precipitation analyses: Development and applications. *19th Conf. on Hydrology*, San Diego, CA, Amer. Meteor. Soc., 1.2, <https://ams.confex.com/ams/pdfpapers/83847.pdf>.
- Mass, C., 1981: Topographically forced convergence in western Washington State. *Mon. Wea. Rev.*, **109**, 1335–1347, [https://doi.org/10.1175/1520-0493\(1981\)109<1335:TFCIWW>2.0.CO;2](https://doi.org/10.1175/1520-0493(1981)109<1335:TFCIWW>2.0.CO;2).
- , N. Johnson, M. Warner, and R. Vargas, 2015: Synoptic control of cross-barrier precipitation ratios for the Cascade

- Mountains. *J. Hydrometeor.*, **16**, 1014–1028, <https://doi.org/10.1175/JHM-D-14-0149.1>.
- Mechem, D. B., Y. L. Kogan, and D. M. Schultz, 2010: Large-eddy observation of post-cold-frontal continental stratocumulus. *J. Atmos. Sci.*, **67**, 3368–3383, <https://doi.org/10.1175/2010JAS3389.1>.
- Medina, S., E. Sukovich, and R. A. Houze, 2007: Vertical structure of precipitation in cyclones crossing the Oregon Cascades. *Mon. Wea. Rev.*, **135**, 3565–3586, <https://doi.org/10.1175/MWR3470.1>.
- Minder, J. R., D. R. Durran, G. H. Roe, and A. Anders, 2008: The climatology of small-scale orographic precipitation over the Olympic Mountains: Patterns and processes. *Quart. J. Roy. Meteor. Soc.*, **134**, 817–839, <https://doi.org/10.1002/qj.258>.
- , —, and —, 2011: Mesoscale controls on the mountain-side snow line. *J. Atmos. Sci.*, **68**, 2107–2127, <https://doi.org/10.1175/JAS-D-10-05006.1>.
- Neiman, P. J., F. M. Ralph, A. B. White, D. E. Kingsmill, and P. O. G. Persson, 2002: The statistical relationship between upslope flow and rainfall in California's coastal mountains: Observations during CALJET. *Mon. Wea. Rev.*, **130**, 1468–1492, [https://doi.org/10.1175/1520-0493\(2002\)130<1468:TSRBUF>2.0.CO;2](https://doi.org/10.1175/1520-0493(2002)130<1468:TSRBUF>2.0.CO;2).
- Picard, L., and C. Mass, 2017: The sensitivity of orographic precipitation to flow direction: An idealized modeling approach. *J. Hydrometeor.*, **18**, 1673–1688, <https://doi.org/10.1175/JHM-D-16-0209.1>.
- Reinecke, P. A., and D. R. Durran, 2008: Estimating topographic blocking using a Froude number when the static stability is nonuniform. *J. Atmos. Sci.*, **65**, 1035–1048, <https://doi.org/10.1175/2007JAS2100.1>.
- Richard, E., N. Chaumerliac, J. F. Mahfouf, and E. C. Nickerson, 1987: Numerical simulation of orographic enhancement of rain with a mesoscale model. *J. Climate Appl. Meteor.*, **26**, 661–669, [https://doi.org/10.1175/1520-0450\(1987\)026<0661:NSOOEO>2.0.CO;2](https://doi.org/10.1175/1520-0450(1987)026<0661:NSOOEO>2.0.CO;2).
- Seo, B.-C., B. Dolan, W. F. Krajewski, S. A. Rutledge, and W. Petersen, 2015: Comparison of single- and dual-polarization-based rainfall estimates using NEXRAD data for the NASA Iowa Flood Studies Project. *J. Hydrometeor.*, **16**, 1658–1675, <https://doi.org/10.1175/JHM-D-14-0169.1>.
- Siler, N., and D. Durran, 2016: What causes weak orographic rain shadows? Insights from case studies in the Cascades and idealized simulations. *J. Atmos. Sci.*, **73**, 4077–4099, <https://doi.org/10.1175/JAS-D-15-0371.1>.
- Smith, J. A., and W. F. Krajewski, 1993: A modeling study of rainfall rate-reflectivity relationships. *Water Resour. Res.*, **29**, 2505–2514, <https://doi.org/10.1029/93WR00962>.
- Smith, R. B., 1989: Hydrostatic flow over mountains. *Advances in Geophysics*, Vol. 31, Academic Press, 1–41, [https://doi.org/10.1016/S0065-2687\(08\)60052-7](https://doi.org/10.1016/S0065-2687(08)60052-7).
- , and I. Barstad, 2004: A linear theory of orographic precipitation. *J. Atmos. Sci.*, **61**, 1377–1391, [https://doi.org/10.1175/1520-0469\(2004\)061<1377:ALTOOP>2.0.CO;2](https://doi.org/10.1175/1520-0469(2004)061<1377:ALTOOP>2.0.CO;2).
- Steenburgh, W. J., 2003: One hundred inches in one hundred hours: Evolution of a Wasatch Mountain winter storm cycle. *Weather Forecasting*, **18**, 1018–1036, [https://doi.org/10.1175/1520-0434\(2003\)018<1018:OHIOH>2.0.CO;2](https://doi.org/10.1175/1520-0434(2003)018<1018:OHIOH>2.0.CO;2).
- Surcel, M., I. Zawadzki, and M. Yau, 2014: On the filtering properties of ensemble averaging for storm-scale precipitation forecasts. *Mon. Wea. Rev.*, **142**, 1093–1105, <https://doi.org/10.1175/MWR-D-13-00134.1>.
- Thompson, G., P. R. Field, R. M. Rasmussen, and W. D. Hall, 2008: Explicit forecasts of winter precipitation using an improved bulk microphysics scheme. Part II: Implementation of a new snow parameterization. *Mon. Wea. Rev.*, **136**, 5095–5115, <https://doi.org/10.1175/2008MWR2387.1>.
- Westrick, K., C. Mass, and B. Colle, 1999: The limitations of the WSR-88D radar network for quantitative precipitation measurement over the coastal western United States. *Bull. Amer. Meteor. Soc.*, **80**, 2289–2298, [https://doi.org/10.1175/1520-0477\(1999\)080<2289:TLOTWR>2.0.CO;2](https://doi.org/10.1175/1520-0477(1999)080<2289:TLOTWR>2.0.CO;2).
- Zishka, K. M., and P. J. Smith, 1980: The climatology of cyclones and anticyclones over North America and surrounding ocean environs for January and July, 1950–77. *Mon. Wea. Rev.*, **108**, 387–401, [https://doi.org/10.1175/1520-0493\(1980\)108<0387:TCOCOA>2.0.CO;2](https://doi.org/10.1175/1520-0493(1980)108<0387:TCOCOA>2.0.CO;2).